Title:	**Experimental evaluation of carbon fibre, fibreglass and aramid tubular braided composites under combined tension-torsion loading**
Article type:	**Full length article**

Abstract

Braided composites are a class of composite materials that feature an inter-woven structure that improves structural stability and damage tolerance. Presently, braided composites under tension and torsion loading have been studied individually. Mechanical behaviour of braided composites under combined tension-torsion loading is common and therefore requires investigation. In this study, mechanical properties of carbon fibre, fibreglass and aramid 2D tubular braided composites (TBCs) were assessed and compared under coupled tension-torsion loading. The plane stress theory investigated the failure mechanism of braids. A contact-free three-dimensional digital image correlation (3D DIC) technique was used to derive detailed and continuous strain maps and understand the buckling behaviour of TBCs.

Keywords: Braided composites, combined loading, 3D digital image correlation

Corresponding Author: Garrett Melenka   **Email**: gmelenka@yorku.ca

Corresponding Author's institution: York university

Department of Mechanical Engineering, 433C, Bergeron Center for Engineering Excellence, 4700 Keele St., North York, ON, M3J 1P3

Order of Authors: Abbas Armanfard, Garrett Melenka

Suggested reviewers: Pierre Mertiny (pmertiny@ualberta.ca), Pascal Hubert (pascal.hubert@mcgill.ca), Frank Ko (frank.ko@ubc.ca)

1. Introduction

Composites materials are utilized for their high strength to weight ratio in industries that require high-performance components [1]–[3]. However, conventional composite laminates suffer

from relatively low toughness and delamination. Moreover, the laminate manufacturing process is costly and time-consuming [4], [5]. In contrast, braided composites have modified characteristics that overcome technical challenges created by conventional laminated composites. Braided composites are a composition of continuously interlaced fibres in a resin epoxy matrix. Braided preforms are produced with an automated braiding process. Braided composites' interwoven nature results in damage tolerance and structural stability [1], [6]. Utilizing lightweight fibres and benefiting from braiding technology as a time and cost-efficient manufacturing method reduces carbon dioxide emissions and answers the increasing demand for high-performance structures such as jet engine stator vanes, fan blades and shafts [1], [7]–[11].

The braided composites typically are produced in tubular cross-section and can be utilized to fabricate axisymmetric parts. Therefore, the evaluation of braided composites in the tubular configuration is required under loading [12], [13]. Braids are formed by interlacing yarns around a mandrel using a Maypole or radial braiding machines [7], [14]. Regular (2/2) patterns are the most common pattern used for manufacturing braids, similar to a twill weave for textile composites, though in bias direction [15]. Different types of fibres have been used for braided composite manufacturing [1]. The most common fibres for manufacturing braided composites are carbon fibre, fibreglass and aramid [16].

Braided composites are becoming more widely adopted for industrial applications; therefore, understanding their mechanical behaviour under various stress states is crucial to avoid premature failure [12]. Independent studies of 2D TBCs under tension and torsion loadings have been investigated by several researchers [5], [6], [17]–[21]. For example, Harte and Fleck investigated fibreglass TBCs to understand and model their deformation and fracture responses in various braiding angles under tensile loading [5]. They found that for TBCs, failure occurs due to fibre fracture for small braid angles, and braid fails because of neck propagation for large braid angles. They used conventional strain gauges to measure deformations. In another work by Harte and Fleck, they studied a regular fibreglass TBC to explore the failure modes for different braid angles under various types of loadings with a minor focus on combined tension-torsion loading [18]. They used conventional strain gauges to perform strain measurements without any discussion on strain distribution over the braid. Chai *et al.* conducted a comprehensive study on carbon fibre TBCs in torsion loading using X-ray computed tomography (CT) imaging to explore the extent of the

damage mechanism of braided structure [20]. Presently, 2D TBCs under tension and torsion loading have been studied individually. Research works have investigated other types of composites under simultaneous tension and torsion loading [22], [23]. Yu *et al*. experimentally investigated a needled composite under coupled tension-torsion loading [22]. Amijima *et al.* conducted static and mechanical fatigue tests for woven glass fabric composite under biaxial tension-torsion loading [23]. Braided composite components frequently experience combined tension-torsion loading while in operation; however, no studies have investigated braids' mechanical properties due to the effect of combined loading [24]. Bike frames, golf clubs and fan blades are an example where braided composite manufacturing is utilized. These structures experience couples and loadings in various directions simultaneously and are examples of when combined loading stress states occurs.

Deformation measurements of braided composites under loading have been performed using different techniques. Many researchers have used a conventional technique such as strain gauges and extensometers for evaluating deformations [4], [5], [18], [22]. However, recently scholars [24]–[29] have turned into the use of digital image correlation (DIC) as a contact-free full-field measurement technique that does not have the limitation regarding material type and specimen size [30]. This technique is called either 2D DIC if the measurement is performed using a single camera or 3D DIC if multiple cameras do the imaging for measurements. 2D DIC is applicable for full-field strain measurements for flat specimens [31], [32]. For TBCs, 3D DIC is preferred as the braids have wavy surfaces and curved structures; therefore, in-plane and out of plane displacement measurement is required [12]. 3D DIC measurement technique is preferred over conventional discrete measurement methods such as strain gauges since it can process strains over multiple unit cells [6], [17]. 3D DIC measurement technique has been used to evaluate tension, torsion and bending individually by our research group [6], [12]. Currently, 3D DIC measurement to study TBCs under combined loading has not been performed.

This study aims to investigate the mechanical behaviour of TBCs under combined tension-torsion loading. The mechanical properties of carbon fibre, fibreglass and aramid TBCs will be assessed as a case study. First, pure tensile experiments will be performed on similarly manufactured TBCs to measure more mechanical characteristics of manufactured TBCs. Data obtained from the tensile loading experiments were used to inform combined loading experiments.

The 3D DIC measurement technique is utilized to examine elastic and failure strain fields and buckling behaviour of TBCs under combined loading. The braid failure mechanism under combined loading is investigated by the plane stress theory of mechanics of material. Stiffness magnitudes are compared for different braids with different types of fibre. The results presented in this case study can evaluate numerical and analytical models for predicting TBCs mechanical behaviour under combined loading.

2. Experimental methods

2.1 *Sample manufacturing*

Braid samples were manufactured using carbon fibre (2", 7.5 oz/sq yd, 3K, FibreGlast Developments CORP, Brookville, Ohio), fibreglass (2", 10.4 oz./sq yd, 0.011" Thick, FibreGlast Developments CORP, Brookville, Ohio), and aramid (2", 9.9 oz./sq yd, 0.018" Thick, FibreGlast Developments CORP, Brookville, Ohio) biaxial sleeves in Regular (2/2) braiding pattern

Braid preforms were manually impregnated with an epoxy resin system (2000 epoxy resin with 2060 hardener, FibreGlast Developments CORP, Brookville, Ohio). Each sleeve was pulled over a steel mandrel (1566 Carbon Steel McMASTER-CARR, Elmhurst, IL) of 38.08 mm (1.5") diameter coated with a mold release (LOCTITE® FREKOTE 770-NC™, Henkel Canada Corporation, Mississauga, Ontario) and then impregnated by resin-hardener with a weight mixing ratio of 100:27. Average properties of braid preforms and resin-hardener used for manufacturing braided composites are listed in Table 1 and Table 2, respectively.

Table 1. Reported averaged properties of braid preforms used for manufacturing braided composites [1], [33]

	Number of yarns in the braid	Longitudinal elastic modulus (GPa)	Ultimate Tensile Strength σ_{UTS} (GPa)	Density ρ (g/cm^3)	Yield (kg/m)	Fabric weight (g/m^2)
Carbon fibre	144	236.14	4.3	1.75	24.7	254.3
Fibreglass	144	72	3.5	2.57	26.5	352.6
Aramid (Kevlar 49)	120	125 ± 13	3.6	1.44	18.7	336

Table 2. Mechanical properties for cured resin-hardener (2000 series resin with 2060 hardener, FibreGlast)

Mechanical Properties	Reported data

Longitudinal elastic modulus (GPa)	2.9
Ultimate tensile strength σ_{UTS} (MPa)	67.7
Density ρ (g/cm³)	1.11

During the resin impregnation process of the braided samples, the impregnated preform was covered with a release fabric ply (Airtech Bleederlease, Composites Canada, Canada). After, the braid was wrapped with 31.75 mm (1.25") heat shrink tape (Airtech Dahlar A575RC Shrink Tape, Composites Canada, Canada) while the mixture of resin-hardener was still in its pot life. Using a heat gun (Model No. HG1300, Black & Decker, China), the tape wrapped over the braided preform was shrunk, and excess resin squeezed out of the braid without leaving any trace of tape due to the use of release fabric. The schematic of the manufacturing process is demonstrated in Figure 1. The impregnated braids were cured at room temperature after 24 hours. This manufacturing technique was used to ensure even compaction of the braid samples. A total of eighteen samples were manufactured, six of each type of preforms. Three of each type of preform was tested in tensile loading experiments, and the three left were used for combined loading experiments. Braided composites were cut into 317.5mm (12.5") as the final length using a cut-off saw (Mecatome T260, PRESU, France).

(4) Shrink tape

(3) Release fabric
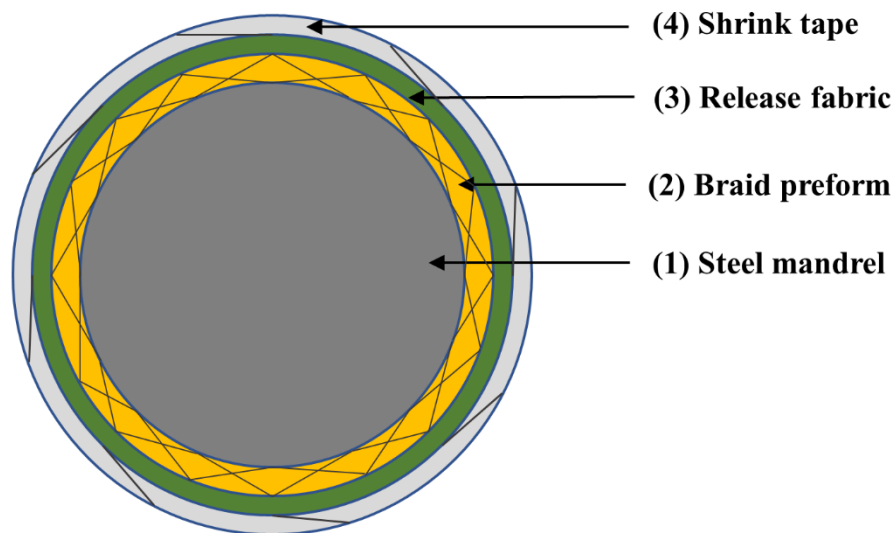
(2) Braid preform

(1) Steel mandrel

Figure 1: Schematic illustration of the manufacturing process. Steps of manufacturing are: 1) coating steel mandrel with mold release. 2) overlaying preform on the mandrel and impregnating it. 3) applying release fabric. 4) wrapping the shrink tape over the braid. Colour should be used in the print version.

2.2 *Specimen geometry measurement*

The outer diameter (D_o) of braided composite samples were measured at five equally spaced locations along the longitudinal direction on braid using a micrometer (25.4–50.8 mm Micrometer, Starrett 3732XFL-2 Inch, Athol, MA). The inner diameter (D_i) was considered the same as the outer diameter of the steel mandrel. The braid unit cell, shown in Figure 2, represents the architecture of the entire composite [34]. Braid angle (θ_b) is the angle between longitudinal and fibre direction of braid. Yarn width (W_y) is a geometric factor that affects the geometry of braided composite. Braid angle and yarn width, illustrated in Figure 2, are two parameters that significantly affect the mechanical properties of braided composites [35], [36] and are commonly measured and reported in studies [12], [19], [37], [38] on braided composites. Braid angle and yarn width were measured on digital images captured from braids in five locations along the braid's longitudinal direction using an image processing software (ImageJ, National Institutes of Health, Bethesda, MD). For this purpose, each braid was photographed five times using a high-resolution camera (Ace acA2440-35um Monochrome USB 3.0, Basler Inc., Exton, PA) equipped with a macro lens (Model No. MLM-3XMP, 2/3" 3.3X Macro Zoom, Computar, US). For fibre volume fraction (v_F) measurements, initial fibre mass and the braid mass were weighed using a high accuracy scale (Model No. ML304T/00, METTLER TOLEDO, Canada). Then the matrix mass was determined from Equation (1). In this equation, m_m, m_b, and m_f are matrix mass, braid mass and fibre mass, respectively.
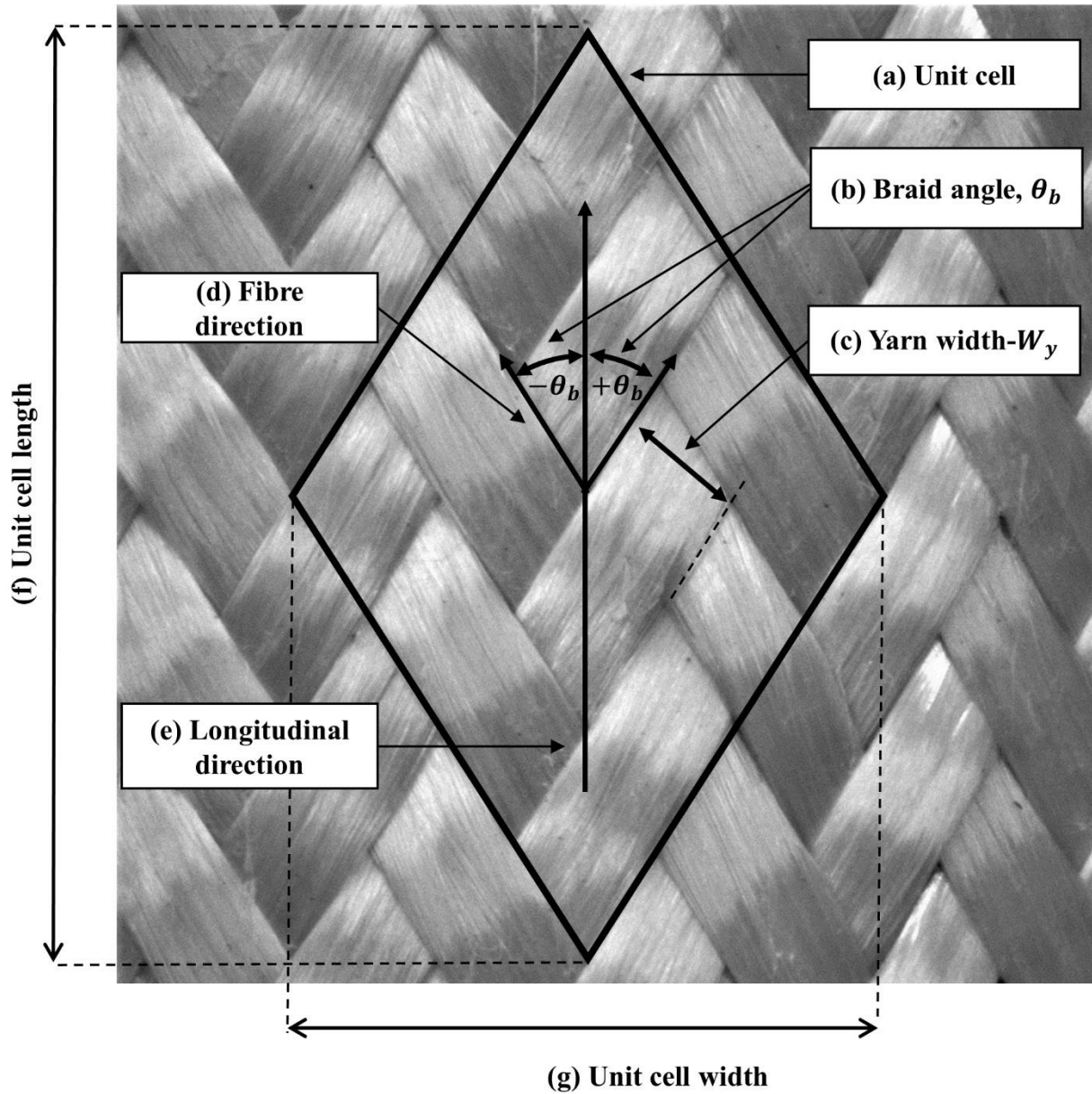
Figure 2: Schematic illustration of braid's unit cell and its geometrical parameters. This figure shows a) unit cell of a regular braid, b) braid angle, c) yarn width, d) fibre direction, e) longitudinal direction of braid, f) unit cell length and g) unit cell width.

$$m_m = m_b - m_f \qquad (1)$$

2.3 *Mounting specimens on tabs*

The braids were bonded to end tabs (Figure 3) made of cold-rolled steel C1045 using a high strength two-part epoxy (Loctite E- 20HP; Hysol, Henkel, Rocky Hill, Co.). End tabs were used to avoid stress concentration and radial deformation on specimens due to the test frame's grips. The end tabs had a 1.5° tapered portion to provide a sufficient gap for the epoxy, similar to methods

in [19], [39]. After placing tabs in the braid, 203.2 mm (8") of braids remains contact-free, which will experience evenly distributed loading in mechanical tests. Bonded tabs were rested on an angle steel bracket and fastened at both ends for 24 hours until the high strength epoxy cures. The use of angle brackets and fasteners minimizes end tab misalignment. The assembly of the test specimen and the angle bracket setup is shown in Figure 3.
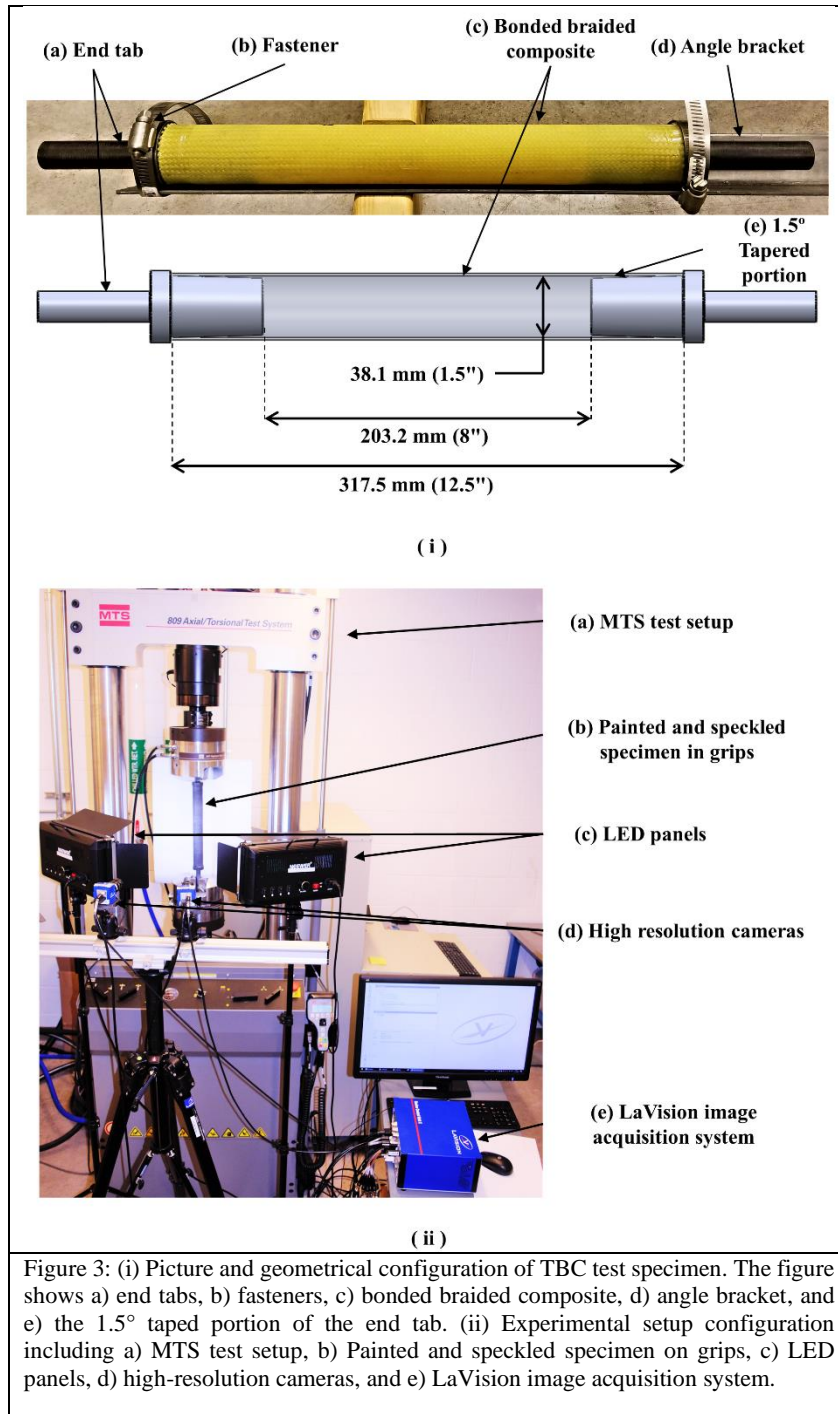
Figure 3: (i) Picture and geometrical configuration of TBC test specimen. The figure shows a) end tabs, b) fasteners, c) bonded braided composite, d) angle bracket, and e) the 1.5° taped portion of the end tab. (ii) Experimental setup configuration including a) MTS test setup, b) Painted and speckled specimen on grips, c) LED panels, d) high-resolution cameras, and e) LaVision image acquisition system.

2.4 *Sample mechanical testing*

Carbon fibre, fibreglass, and aramid TBCs were evaluated in combined loading to investigate their strain behaviour, failure mechanism, buckling trend and stiffness characteristic. Three samples were assessed for each braid type. The axial/torsional test frame (809 MTS Systems Corporation, USA) shown in Figure 3 was used to perform combined mechanical loading tests.

Force and torque data were measured using a 100KN axial load and 1100N-m torque capacity load unit (Model number: 319.10, MTS Systems Corporation, USA). Force, torque, displacement, and rotation data were recorded using the test frame's data acquisition system.

The combined loading test consisted of two loading steps. In the first step, each specimen was axially loaded with a constant rate of 1 KN/min as per Yu *et al.* to identical axial stress within the uniaxial elastic limit of all three types of samples[13]. In the second step, the lower crosshead of the test frame begins applying torque load with a constant rotation speed of 0.01°/s until 18° of rotation. During the second step, using the load control mode of the test frame, the axial stress on braids was maintained from the first step.. The combined loading experiment was designed so that braids experience permanent deformation and failure due to increased torque in the second step of loading. The failure in the first step is avoided by applying tensile stress within the uniaxial elastic limit of all three types of specimens. Preloading samples to the same amount of axial stress rather than axial force that was the method used in [13] allows the comparison of the mechanical response of braids in the combined loading test. Therefore, carbon fibre, fibreglass and aramid TBCs will be compared against each other based on their behaviour in the torsion loading step while each specimen is experiencing identical axial tensile stress.

The magnitude of the identical axial stress for the first step of loading will be determined by performing tensile loading experiments on similar braids. For this purpose, three of each carbon fibre, fibreglass, and aramid braided composite samples were evaluated in tensile loading to investigate their stress-strain curves. Moreover, other mechanical behaviours, such as 3D DIC strain fields, necking behaviour, and fracture modes, will be shown to understand better the mechanical characteristics of manufactured TBCs used in this study. As there is no specific standard for TBCs for the tensile loading test, ASTM E111 [40] and D3039 [41] standards were used as a guide for performing the experiments and reporting characteristic parameters such as young modules and fracture modes.

The same test frame shown in was used to perform tensile mechanical tests. Force and displacement data were recorded using the test frame's data acquisition system. The axial load was applied in displacement control mode at a crosshead speed of 1mm/min until complete specimen failure. According to ASTM D3039 [41], this loading rate was chosen with some modifications. Instead of having specimens fail between 1 to 10 min, all samples experienced plastic deformation

within the aforementioned period. This modification was considered to ensure that deformations occur slow enough so that the measurement technique works correctly.

2.5 *Deformation measurement*

The 3D DIC technique performed deformation measurements for tensile and combined loading experiments. 3D DIC allows capturing and tracing braiding patterns and braid yarns during mechanical tests. 3D DIC setup included two high-resolution cameras (LaVision Image M-lite 5M, LaVision GmbH, Göttingen, Germany) with 2464×2056 pixels and a pixel size of 3.45 µm and digital output of 12 bit. The cameras were equipped with 50 mm focal length lenses (NMV-50M23, Navitar, Inc., Rochester, NY). The distance between cameras and specimen was approximately 850 mm. The images were acquired using a commercial software package (DaVis version 10.0.3 StrainMaster, LaVision GmbH, Göttingen, Germany). Two LED panels (Neewer 500 LED Photo Studio Lighting Panel, Shenzhen, China) were used for illuminating specimens while imaging their deformation during loading. According to the sample and camera configuration, a stereo angle of 17° was used. This stereo angle was determined to maximize the usable depth of focus, get an effective field of view (FOV) and reduce out-of-plane uncertainty [30]. The camera setup was designed to have an approximate FOV of 115×94 mm^2 (Figure 4). The braids were positioned in the center of both cameras FOV. A sufficient length of braid was captured using this FOV to compensate for large displacements in tensile tests. The image acquisition rate was 1Hz for tensile loading experiments and 2Hz for the combined loading tests. The difference in image acquisition rate is due to different speeds of tests and the experiment duration. The summary of the imaging setup configuration is listed in Table 3. The experimental test setup is shown in Figure 3-(ii). This figure shows the MTS test frame, mounted specimen, stereo cameras, LED lights and the LaVision imaging system.

Table 3: Image acquisition setting.

Digital image correlation parameters	Settings	
Camera Resolution	2464×2056 pixels	
Camera Pixel Size	3.45 µm	
Digital output	12 bit	
Camera Lenses	2X Navitar 50mm lens	
Distance Between Cameras and Specimen	850 mm	
Stereo Angle of Cameras	17°	
Camera Field of View (FOV)	115×94 mm^2	
Image Acquisition Rate	1Hz for tensile loading tests	2Hz for combined loading tests

2.6   *DIC Sample preparation*

High-quality speckle patterns are required to ensure proper DIC measurements. High contrast speckles allow small subset sizes, which obtain more precise strain fields for samples [42]. A speckling procedure similar to methods used in [12], [19] was followed. An example painted and speckled braid is illustrated in Figure 4-(i). The image intensity variation along the white dashed line in transverse direction of speckled braid is shown in this figure. The portion of image intensity that corresponds to the region of interest, ROI, and the specimen is demonstrated using vertical black dashed lines. This ROI will be used to perform averaging on strain measurements for tensile experiment results. Figure 4-(i) shows that the test samples have sufficient contrast variations that will be suitable for DIC measurement.
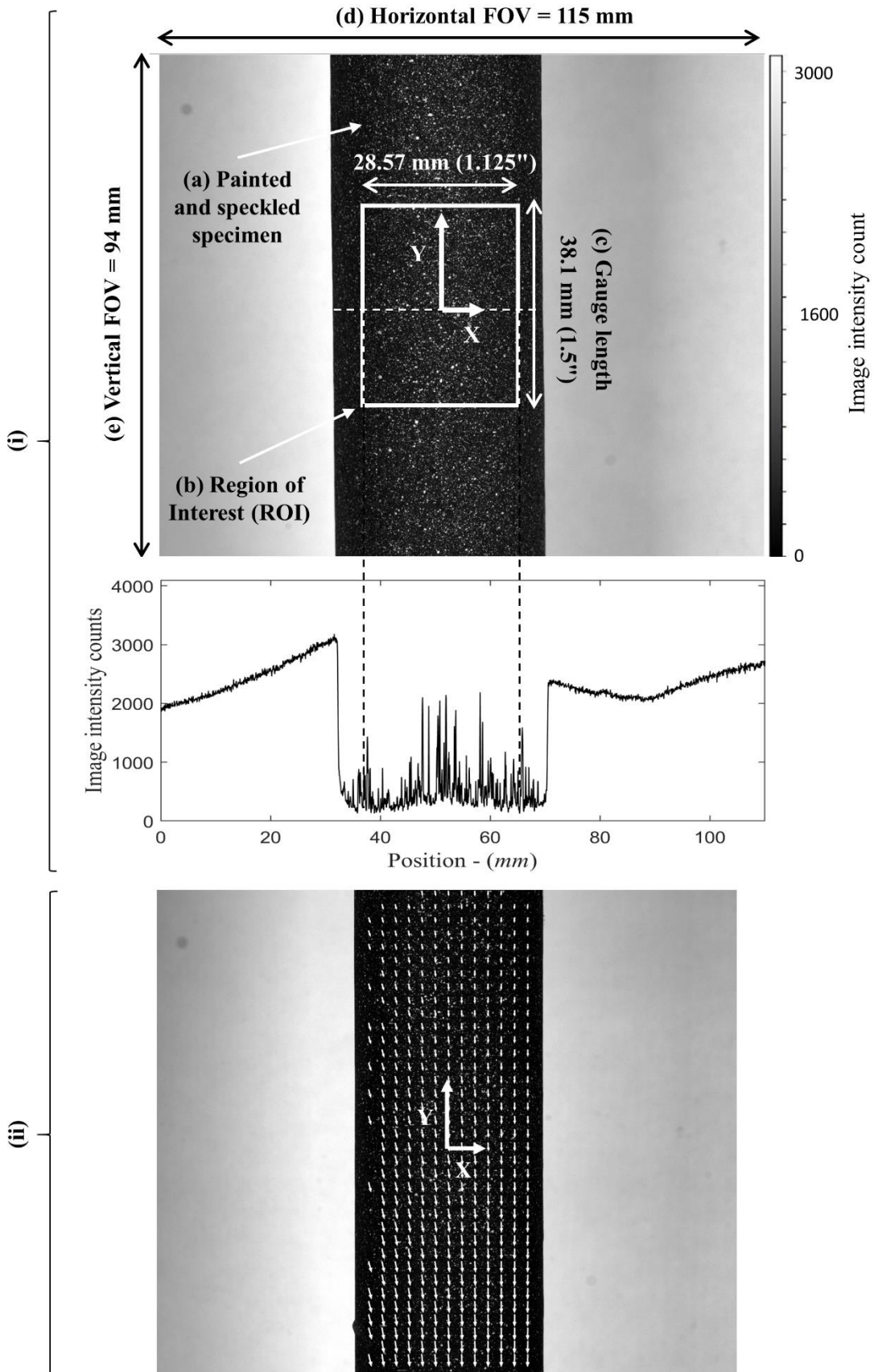
(d) Horizontal FOV = 115 mm

28.57 mm (1.125")

(a) Painted and speckled specimen

(c) Gauge length 38.1 mm (1.5")

Y

X

(b) Region of Interest (ROI)

(e) Vertical FOV = 94 mm

3000

1600

0

Image intensity count

(i)

Image intensity counts

4000

3000

2000

1000

0

0   20   40   60   80   100

Position - (mm)

(ii)

Y

X

Figure 4: (i) A raw image from DIC cameras. This figure shows a) painted and speckled specimen, b) ROI, c) gauge length of braid used for strain measurement, d) horizontal FOV, and e) vertical FOV. The image intensity counts along the transverse direction of the braid is also shown. (ii) Example displacement vector field of a TBC. The vector density has been reduced to 1 in 8 for clarity. The sample coordinate system is shown for the calculation of longitudinal, ϵ_{yy}, and transverse, ϵ_{xx}, strains.

2.7   *3D DIC processing and post-processing*

3D DIC processing of captured images during tensile tests for strain and displacement measurement was completed using a commercial DIC software package (DaVis version 10.0.3 StrainMaster, LaVision GmbH, Gottingen, Germany). To perform 3D DIC, images acquired from both cameras were linked and calibrated using a calibration process. For calibration, a 106×106 mm^2 calibration target (Type 106-10-SSDP, LaVision GmbH, Göttingen, Germany) was placed in the test frame's grips using a holder such that its center would coincide with the center and the front surface of the specimen when the specimen was mounted in the test frame. This way, the braid surface centre would stay in focus and within the FOV of cameras during test stroke.

A least-square optical flow displacement measurement algorithm was used to drive displacement vector fields (Figure 4-(ii)) using DIC processing software [43]. A subset window size of 21×21 pixels and a step size of 7 pixels were used to perform a correlation between images. Selecting a 38.10×28.57 mm^2 ROI (1.5×1.125 inch^2) and using processed displacement vector fields in the ROI, the averaged longitudinal strain, ϵ_{yy}, and transverse strain, ϵ_{xx}, in a gauge length of 38.10 mm (1.5") (Figure 4-(i)) were calculated during test stroke for tensile experiments. ASTM D3039 was used as a guide to determine the gauge length [41]. According to a study by Naik *et al.* [44], the ROI must be larger than the braid unit cell to produce consistent strain results. The ROI in Figure 4 is large enough to ensure bulk strain is measured over multiple unit cells since the average unit cell length and width (Figure 2) for all three types of braids are 9.13 mm ± 0.88 mm and 5.27 mm ± 0.03 mm, respectively. The 3D DIC analysis parameters are summarized in Table 4.

Table 4. Digital image correlation settings.

3D DIC parameters	Settings
Image Scale Factor	21 pixels/mm
Correlation Subset Size	21×21 pixels
Correlation Step Size	7 pixels
Region of Interest (ROI)	38.10×28.57 mm^2 (1.5×1.125 inch^2)
Gauge Length	38.10 mm (1.5")

2.8 *Principal planes of braid*

According to the mechanics of materials theory, since the braids examined in this study are thin-walled tubes and $\sigma_z = \tau_{zx} = \tau_{zy} = 0$, the state of plane stress is assumed to exist in this study [45], [46], although the TBC structure is non-isotropic. According to these assumptions, principal planes and stresses of TBCs under combined loading are investigated in this work.

Figure 5-(i) shows a representative element of braid oriented in x-y coordinates under combined tension-torsion loading at point Q. This figure illustrates that the braid element is experiencing a constant positive longitudinal stress in the y-direction, σ_y, during the rotational step of the combined loading experiment. Figure 5-(i) also shows negative shear stress, τ_{xy}. The negative sign of shear stress is due to direction of applied torque from the lower crosshead. Figure 5-(ii) shows the same element oriented in principal planes. The principal planes of stresses at point Q are the planes of θ_{P_1} and θ_{P_2} obtained from Equation (2).

$$\theta_{P_{1,2}} = \frac{tan^{-1}(\frac{2\tau_{xy}}{\sigma_x - \sigma_y})}{2} \qquad (2)$$

The principal planes are 90° apart from each other so that $\theta_{P_2} = \theta_{P_1} + 90°$. These planes contain the faces of the element.

Figure 5-(ii) also shows principal stresses, σ_1 and σ_2, which are acting perpendicular to element faces and along with principal directions of 1 and 2. When the representative element is in the orientation of principal planes, only two axial stresses, σ_1 and σ_2, are exerted on the faces of the

15

element. The element experiences no shear stress when it is rotated to principal planes since the plane stress condition dominates. From Equations (3) and (4), the magnitude and sign of principal stresses along principal directions of 1 and 2 are determined. In these two equations, transverse stress, σ_x, is not included since it is zero at all time as there was no load exerted to the specimen in the horizontal direction.
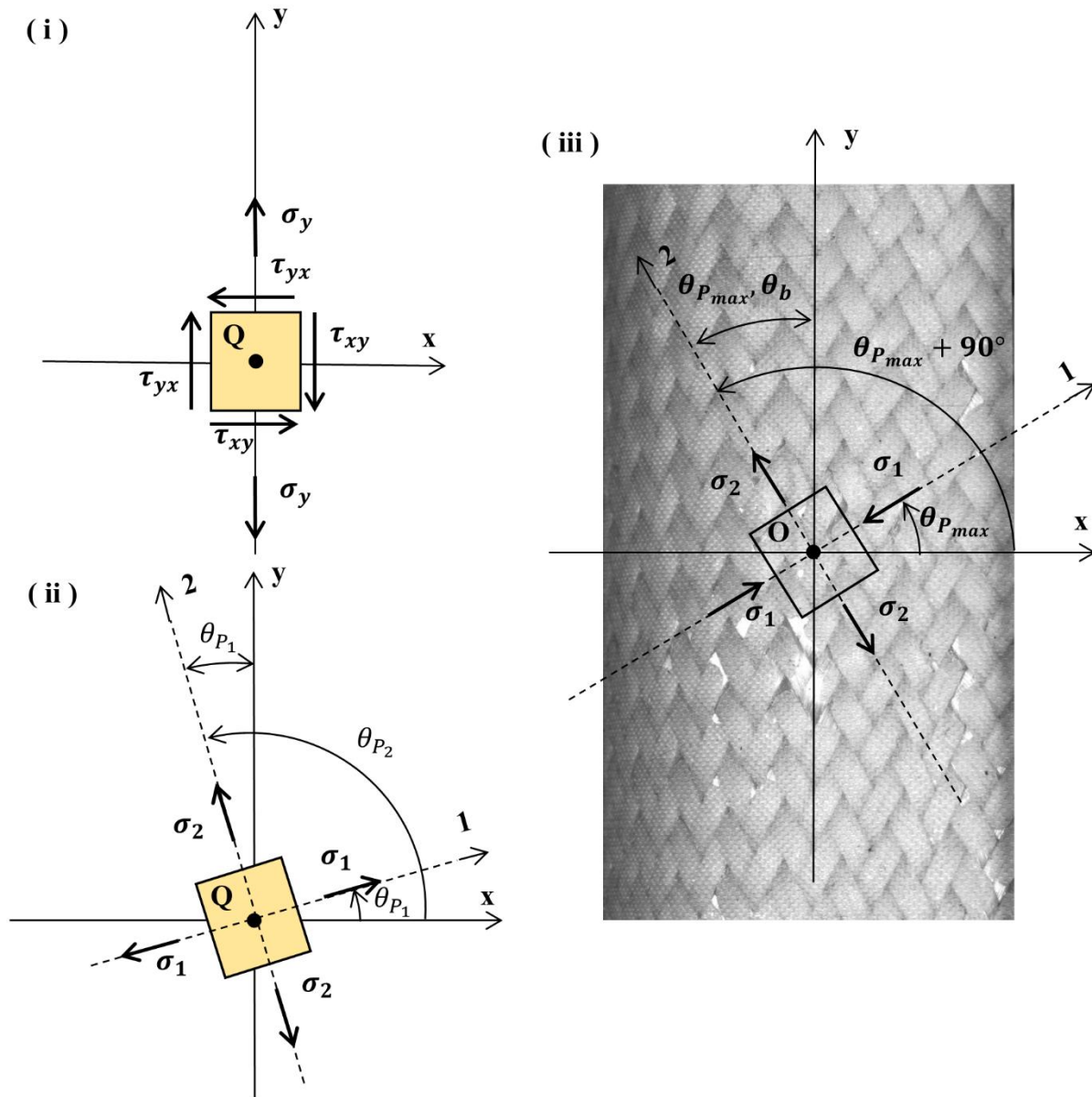
Figure 5: Figure (i) shows the stresses on the braid element Q under loading oriented in x-y coordinates. Figure (ii) shows the same element of the figure (i) oriented in principal directions and their corresponding principal stresses. Figure (iii) illustrates principal planes and stresses on an example element of the braid at point O while the braid is at its maximum shear stress at $\theta_{P_1} = \theta_{p_{max}} = \theta_b$.

$$\sigma_1 = \frac{\sigma_y}{2} - \frac{\sigma_y}{2} \cos 2\theta_{P_1} + \tau_{xy} \sin 2\theta_{P_1} \qquad (3)$$

$$\sigma_2 = \frac{\sigma_y}{2} + \frac{\sigma_y}{2} \cos 2\theta_{P_1} - \tau_{xy} \sin 2\theta_{P_1} \qquad (4)$$

3. Results and discussion

3.1 *Braid geometry analysis*

The inner (D_i) and outer (D_o) diameters of all manufactured TBCs were physically measured using a high accuracy micrometer. The diameter measurements were used to determine cross-sectional areas of braids. Braid angle (θ_b) was accurately measured using a high-resolution camera equipped with a macro lens and ImageJ software. Yarn width (W_y) was also optically measured technique for braid angle measurement. The average value and the standard deviation of inner diameter, outer diameter, braid angle, and braid yarn width measurements for tensile and combined loading test specimens are listed in Table 5 and Table 6. Inner diameters of braids were considered the same as the mandrel's outer diameter and had minimal variation due to the mandrel surface finish.

Having densities from Table 1 and Table 2 and using measured fibre mass (m_f) and matrix mass (m_m) listed in Table 5 and Table 6, fibre volume (V_f) and matrix volume (V_m) were calculated using Equations (5) and (6). In these equations, ρ_f and ρ_m are the fibre and matrix densities, respectively. Using calculated fibre (V_f) and matrix (V_m) volumes, fibre volume fraction (v_F) measurements were performed using Equation (7). The averaged fibre volume fraction with its standard deviation for three group of braids is summarized in Table 5 and Table 6. According to [1], the fibre volume fraction for typical laminates is between 50% to 70% and can be lower for braided composites. Considering all specimens for both types of experiments, the fibre volume

fraction measured for the manufactured TBCs in this study is lower than 42%, which agrees with the expectations in [1].

$$V_f = \frac{m_f}{\rho_f} \tag{5}$$

$$V_m = \frac{m_m}{\rho_m} \tag{6}$$

$$v_F = \frac{V_f}{V_f + V_m} \tag{7}$$

Table 5. Average geometrical properties with ± standard deviations for manufactured braids for tensile loading experiments.

Braid type	Inner diameter D_i (mm)	Outer Diameter D_o (mm)	Braid angle θ_b (degree)	Braid yarn width W_y (mm)	Fibre mass m_f (g)	Matrix mass m_m (g)	Fibre volume fraction v_F (%)
Carbon 3K	38.08 ± 0.00	39.08 ± 0.03	33.63 ± 0.58	1.50 ± 0.09	12.71 ± 0.00	16.12 ± 1.91	33.47 ± 2.53
Fiberglass	38.08 ± 0.00	38.95 ± 0.13	31.55 ± 1.81	1.43 ± 0.04	17.97 ± 0.00	12.84 ± 3.55	38.49 ± 7.15
Aramid (Kevlar 49)	38.08 ± 0.00	39.56 ± 0.12	30.95 ± 0.38	1.71 ± 0.12	17.89 ± 0.32	21.03 ± 3.26	39.83 ± 3.55

Table 6. Average measured properties with ± standard deviations for manufactured braids for combined loading experiments.

Braid type	Inner diameter (mm) D_i	Outer Diameter (mm) D_o	Braid angle (degree) θ_b	Braid yarn width (mm) W_y	Fibre mass (g) m_f	Matrix mass (g) m_m	Fibre volume fraction (%) v_F
Carbon 3K	38.08 ± 0.00	39.05 ± 0.04	32.48 ± 0.93	1.53 ± 0.12	12.72 ± 0.01	15.72 ± 1.6	34.03 ± 2.37
Fiberglass	38.08 ± 0.00	39.05 ± 0.06	30.83 ± 1.13	1.40 ± 0.06	17.97 ± 0.01	14.70 ± 1.85	34.72 ± 2.98
Aramid (Kevlar 49)	38.08 ± 0.00	39.67 ± 0.33	32.83 ± 0.11	1.71 ± 0.06	17.67 ± 0.05	19.73 ± 2.54	41.01 ± 3.30

The outer diameter of braids was also calculated using surface height data extracted from 3D DIC results. A similar approach was performed by Leung *et al.* [47]. Using a circle fitting function [48], five circles were fitted on surface height data to get five outer diameter measurements for each braid. Figure 6 shows an example fitted circle on 3D DIC height data. In this figure, the reconstructed surface from 3D DIC data has formed a semicircle and is shown by line (i). Line (ii) in this figure shows the fitted circle on 3D DIC data of line (i). This fitted circle's diameter was considered the outer diameter of braid measured from 3D DIC results.
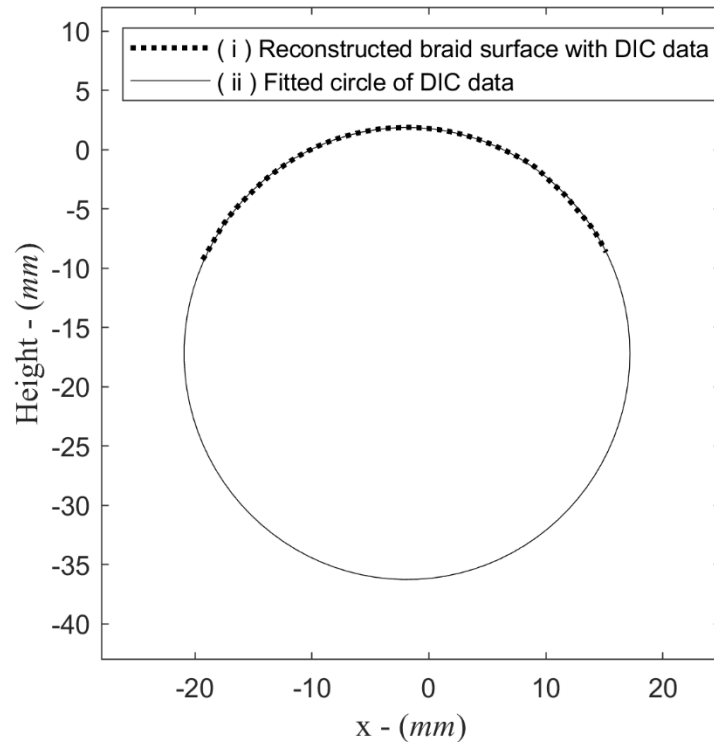
Figure 6: An example of outer diameter measurement of the braid using circle fitting on 3D DIC result.

For validating the accuracy of 3D DIC measurements, the fitted outer diameter measurements were compared with the physically measured outer diameter with the micrometer. This comparison indicates that stereo cameras were correctly placed and calibrated and ensures that strain and displacement measurements with the 3D DIC technique has high accuracy. A similar comparison for 3D DIC accuracy validation was made in [6]. Table 7 compares the outer diameter between physically and optically measurement techniques for all eighteen manufactured samples. This table demonstrates a good match between the measurements. 1.17% is the maximum difference between physically and fitted outer diameter for the braids. The acceptable agreement between physically measured diameters and the diameters from the fitted circle on 3D DIC height data states that the 3D DIC technique was accurate and well-calibrated for all the experiments; therefore, the resulting strain and displacement values of 3D DIC measurement were reliable. According to Table 7, the standard deviation values for diameters of the fitted circles are meaningfully higher than those measured with the micrometer. The main reason is the precision of high-quality images captured with the 3D DIC technique with high-resolution cameras. These images account entirely for the waviness surface of braided composites due to yarn interlacement, while the micrometer cannot

reflect the non-uniform surface of the braid. Therefore, extracted height data from 3D DIC measurements showed variation due to the braid's surface structure's nature and results in a larger magnitude for standard deviations of fitted diameters than the diameters measured physically.

Table 7. Comparison of braid specimen outer diameters measured using physical technique and fitted surface height data of 3D DIC results.

Braid type	Physically measured D_o (mm)	St Dev of physically measured D_o (mm)	D_o of the fitted circle using DIC height data (mm)	St Dev of D_o of the fitted circle using DIC height data (mm)	Difference (%)
Carbon 3K	39.06	0.03	38.23	0.35	1.07
Fiberglass	39.00	0.10	38.27	0.27	0.94
Aramid (Kevlar 49)	39.62	0.23	38.71	0.55	1.17

3.2 *Tensile loading experiments*

3.2.1 *Longitudinal strain and longitudinal modulus*

Full-field strain measurement of tubular braided composites was conducted using the 3D DIC technique. Figure 7 represents an example of 2D images of longitudinal strain distributions on the surface of carbon fibre, fibreglass and aramid braids when experiencing stresses from 40MPa to 250MPa. According to this figure, braids are experiencing inhomogeneous strain distribution due to their interwoven structure. Figure 7 also indicates that when braids are under higher loads, strain magnitude intensifies, illustrated by richer red strain fields. This figure demonstrates the longitudinal strain variations at the 250MPa corresponding to the dark vertical line in the middle of the braid. According to the range of strain variations in this figure, the aramid specimen has the highest magnitudes of strains, and the carbon fibre sample shows the lowest values for strains. The strain's periods shown in Figure 7 corresponds to the period of yarns of the braids. Similar strain distribution observations were seen in 3D DIC studies on different TBCs by Melenka *et al.* [6] and Bossio-Bruni *et al.* [21].
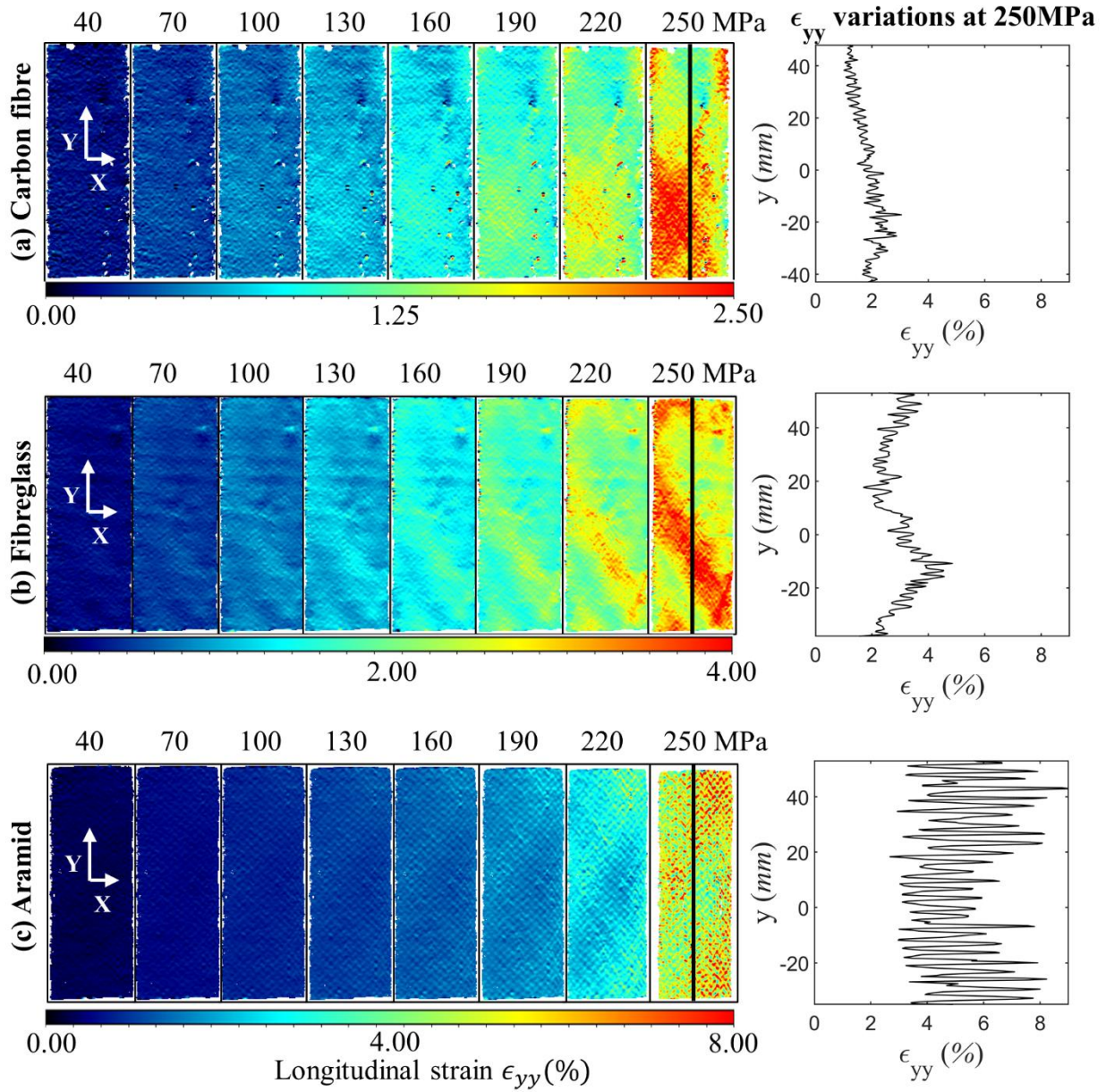
Figure 7: Longitudinal strain distribution on three types of braids for the stress range of 40MPa to 250MPa with increasing steps of 30MPa. Sample images show the two-dimensional strain distribution for the tubular braids (a) Carbon fibre, (b) Fiberglass (c) Aramid. Longitudinal strain distribution along the middle vertical dark line of sample braids at 250MPa stress is plotted.

As illustrated in Figure 7, there is a significant strain variation on the braid's surface due to the yarn undulations in the braided structure. Therefore, the ROI demonstrated in Figure 4-(i) was used to determine an average strain over the surface of the braid. The averaged strain magnitude is used to plot and examine strain curves in this study. This technique is similar to some other studies on 2D braided composites to determine effective strains [6], [12], [32]. The stress-strain curves for all samples tested are shown in Figure 8. In this figure, the stress type is axial stress,

σ_{yy}, and the strain type is longitudinal strain, ϵ_{yy}. Figure 8 shows the full tensile stroke for all braid samples up to failure. According to this figure, stress-strain relation increases almost linearly at the very beginning of the curves for all braids. Therefore, all braids have shown an elastic behaviour at the beginning of the loading process. According to this figure, all braids show some fluctuating and unstable behaviour for higher stresses, indicating permanent deformations for braid specimens. Only one of the samples, aramid braid, experienced an unusual failure process observed as a sharp valley in its stress-strain curve in Figure 8. This behaviour can be due to fibre misalignments and uneven resin distribution, which is common when manual manufacturing techniques are used. Shrink tapes and the release fabrics were used to minimize these manufacturing errors and have been successful for the other eight samples.
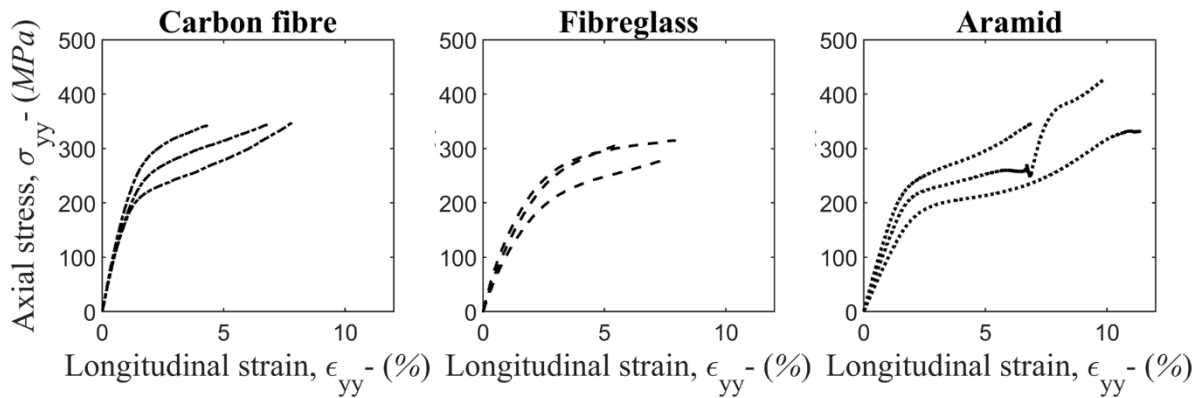
Figure 8: Stress-strain curves for carbon fibre, fibreglass and aramid TBCs in separate frames. The full stroke of tensile tests is shown for all samples.

Figure 9 shows 3D representations of axial strain distributions on the surface of carbon fibre, fibreglass and aramid braids when experiencing three states of low tensile stresses at 20 MPa, 40MPa and 60MPa. This figure shows three stress steps at the beginning of the testing stroke, where braids show excellent linear behaviour in their stress-strain curves shown in Figure 8. Figure 9 demonstrates that strain fields follow the yarn directions of braids. Figure 9 shows negligible localized strain concentration (less than 0.6%) on braids according to strain colour maps, which means for stresses between 20MPa to 60MPa, no failure has occurred in fibre matrix components of braids.
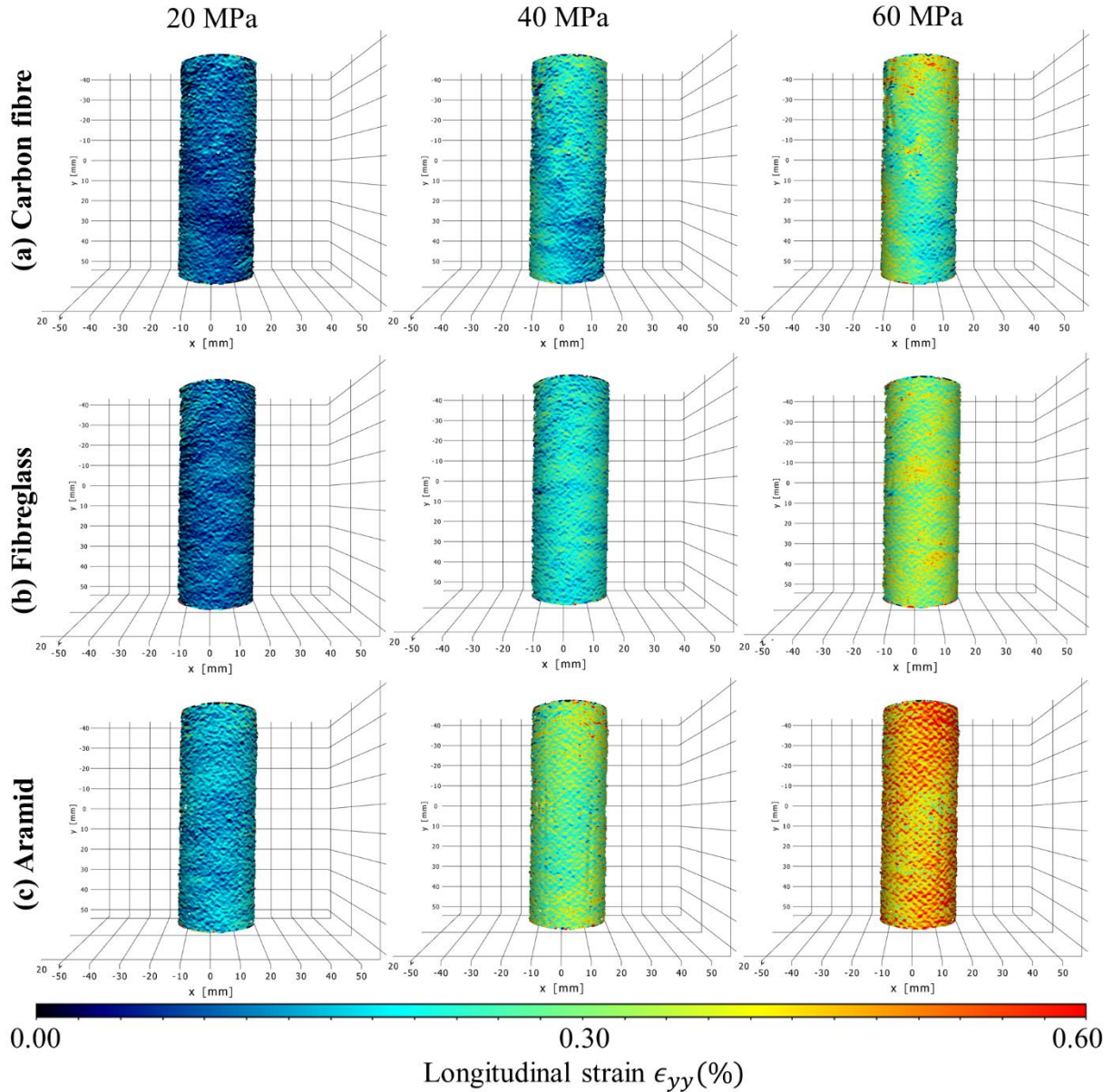
Figure 9: 3D representation of longitudinal strain distribution on three types of brads at low-stress states. Sample images show the three-dimensional strain distribution for the tubular braids (a) Carbon fibre, (b) Fiberglass, (c) Aramid. Sample stress of 20, 40 and 60 MPa are visualized.

The strain behaviour of braids under low-stress states is further discussed using the stress-strain plots of Figure 10. The linear region of stress-strain plots of Figure 8 is separately shown in Figure 10. The stress-strain line for each sample is plotted with high linearity of $R^2 = 0.99$. This figure indicates that for stresses between 20MPa and 60MPa, all the braids completely have elastic behaviour, which agrees with the strain maps demonstrated in Figure 9. The strain maps in Figure 9 do not show any significant localized strain concentrations. Figure 10 indicates that the linear elastic region of the stress-strain plot for carbon fibre and fibreglass braids ends sooner and at

significantly lower strains than aramid braids. Thus, aramid braids can endure larger strain magnitudes than carbon fibre and fibreglass braids and do not show permanent deformations. This observation matched with strain variation plots in Figure 7, which shows much higher axial strain magnitudes for aramid braids than carbon fibre and fibreglass braids.
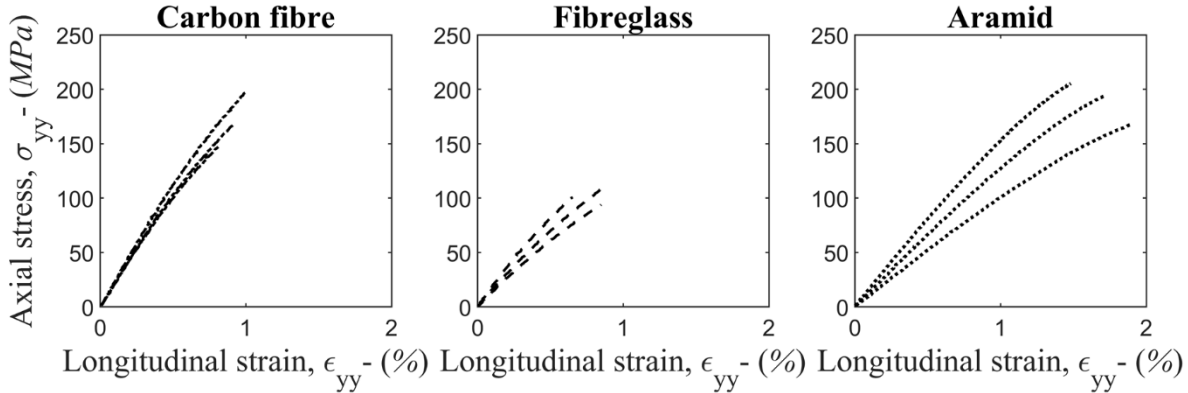
Figure 10: Linear region of stress-strain curves for carbon fibre, fibreglass and aramid TBCs. These curves are used to calculate the longitudinal elastic modulus of different braids.

The stress-strain curves of Figure 10 are used to determine the longitudinal elastic moduli for each of the braid samples. The longitudinal elastic modulus for the material is defined as the slope of the stress-strain plot. The magnitude of longitudinal elastic moduli for carbon fibre, fibreglass and aramid braids are 20.00 ± 0.95GPa, 13.90 ± 2.37GPa and 12.20 ± 2.65GPa, respectively. The decreasing modulus trend among these materials, with carbon having the highest modulus and aramid with the lowest modulus, was also observed by Carey *et al.*[49]. They proposed an analytical model to study the mechanical properties of diamond braided composites and compared their model with some analytical and experimental studied for carbon fibre, fibreglass and aramid braids. Xu *et al.* generated a finite element method to predict the mechanical properties of biaxial and triaxial braids in different braiding patterns for braids with flat unit cells [50]. They have predicted the longitudinal elastic modulus for carbon fibre and fibreglass braids to be 34.34GPa and 22.3GPa, respectively. The predicted values are for biaxial regular braids with the same braiding angles for braids listed in Table 5. The Xu *et al.* results are about 25% higher than the experimental results of this study on carbon fibre and fibreglass. The main reason for this difference can be due to the higher longitudinal modulus of fibre and matrix that were used as the input data for Xu *et al.* model. Comparison of fibre types here is not applicable since the exact type of all fibres is not reported by Xu *et al*. Moreover, their model was designed for braids with a flat unit cell; however, the moduli found in this work are for tubular cross-section braids.

24

Therefore, the difference between the results of Xu *et al.* model and this research study may be due to different cross-sections. Melenka *et al.* [51] introduced an analytical model to anticipate the mechanical properties of TBCs. They have suggested that for an Aramid (Kevlar 49) TBC with a similar braid angle as braids in this study, the longitudinal elastic modulus is about 13.57GPa, similar to what is found for the Aramid braids of this experiment. The slight difference can be due to different geometrical parameters used, such as the number of yarns, yarns width and braid diameter.

3.2.2 *Transverse strain (ϵ_{xx}) and necking*

Like the axial strain distributions previously discussed, transverse strains for carbon fibre, fibreglass and Aramid TBCs are examined here. Figure 11 represents 2D transverse strain distributions of example braids for stresses between 40MPa to 250MPa. This figure indicates that when loading increases on braids, transverse strain magnitude intensifies, illustrated by richer blue shades in strain fields. As the load increases, inhomogeneous stress distribution due to braided composites' interwoven structure becomes more evident. Figure 11 also demonstrates the transverse strain variation of the braids at the 250MPa corresponding to the dark horizontal line in the middle of the braid. The strain period corresponds to the period of yarns of the braids. Similar observations were seen in a 3D DIC study by Melenka *et al*. [6] on TBCs.
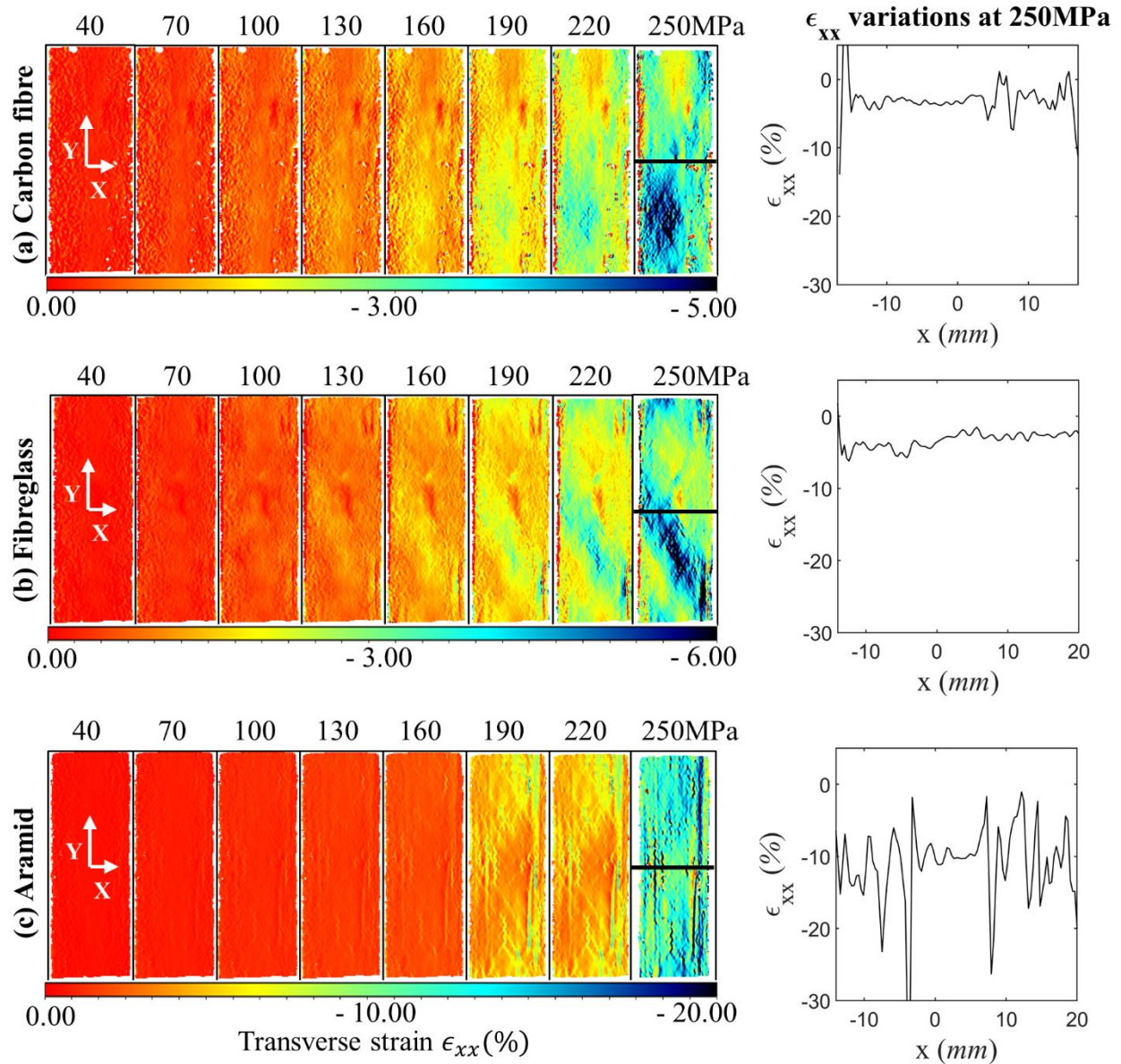
Figure 11: Transverse strain distribution on three types of braids for a stress range of 40 MPa to 250 MPa with increasing steps of 30 MPa. Sample images show the two-dimensional strain distribution for the tubular braids (a) Carbon fibre, (b) Fiberglass, (c) Aramid. Transverse strain distribution along the middle vertical dark line of sample braids at 250 MPa stress is also plotted.

When loading increases and braided composites experience higher loads in tensile tests, strain concentrations become evident, matrix failure occurs, and specimens begin their necking process [6]. Figure 12 demonstrates the necking process of TBCs during tensile loading. In this figure, the surface height of braids corresponds to the horizontal dark line shown in Figure 11. The surface height is plotted during different stress stages from the unloaded specimen at 0MPa, which is the initial curvature of the braid to Ultimate Tensile Stress, σ_{UTS}, at which braids fail. According to Figure 12, all three types of braids show minimal necking at 40MPa by having an almost complete

curvature overlap with the unloaded stage. This observation also matches the strain maps of braids in Figure 11, which do not show significant transverse strain at 40MPa. At the stress of 190MPa, necking has begun and is more evident for aramid braids than carbon fibre and fibreglass specimens. This comparison agrees with the details demonstrated in Figure 11, which shows that larger strain values and sudden changes are strain fields for aramid braids compared to the other two types of braids. Increasing load on braids from 190MPa to 250MPa and ultimate tensile stress, necking grows faster than the increase rate before 190MPa. This higher increase rate is due to the plastic deformation of braids, which occurs for loads higher than 190MPa according to the stress-strain curve in Figure 8.
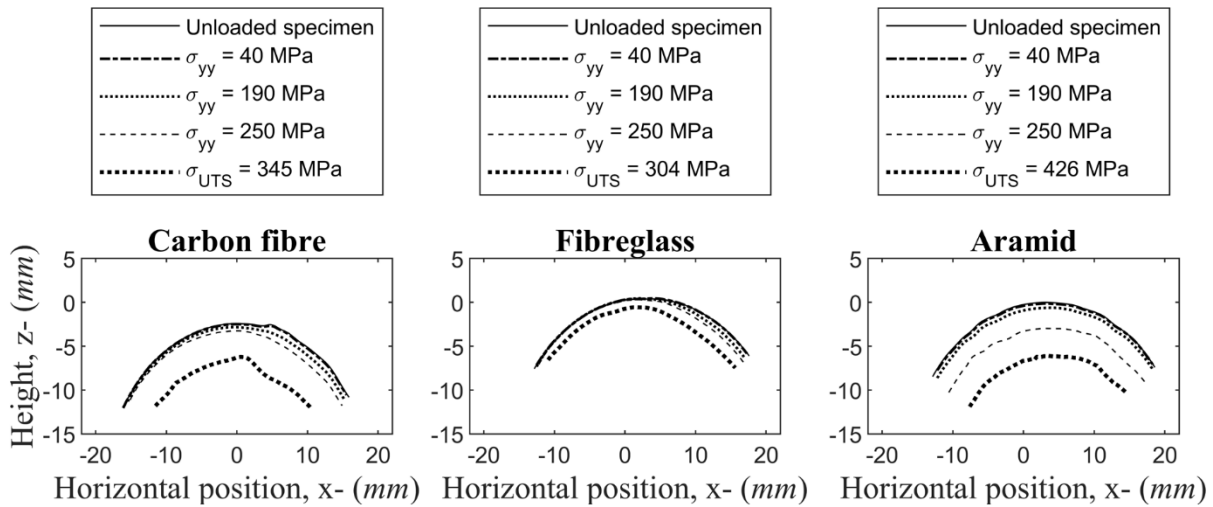
Figure 12: Surface profile of three example braids of each fibre type during complete loading stroke. The necking process of samples is shown for carbon fibre, fibreglass and aramid TBCs.

Similar to Figure 9, Figure 13 shows 3D representations of transverse strain distribution on the braids when experiencing three states of low tensile stresses at 20MPa, 40 MPa and 60 MPa. This figure shows that transverse strain fields on braids follow the yarn pattern of braids. Similar to the longitudinal strain distribution in Figure 9, Figure 13 shows no significant transverse strain concentration on braids surface, which means no failure has occurred in composite constituents, and braids are behaving elastically in this loading span.

According to Figure 9, Figure 10 and Figure 13, 40MPa of axial stress is determined to be within the uniaxial elastic limit of all three types of manufactured TBCs for this study. Therefore, 40MPa will be used to axially preload the composite specimens in combined loading experiments discussed in Section 3.3.
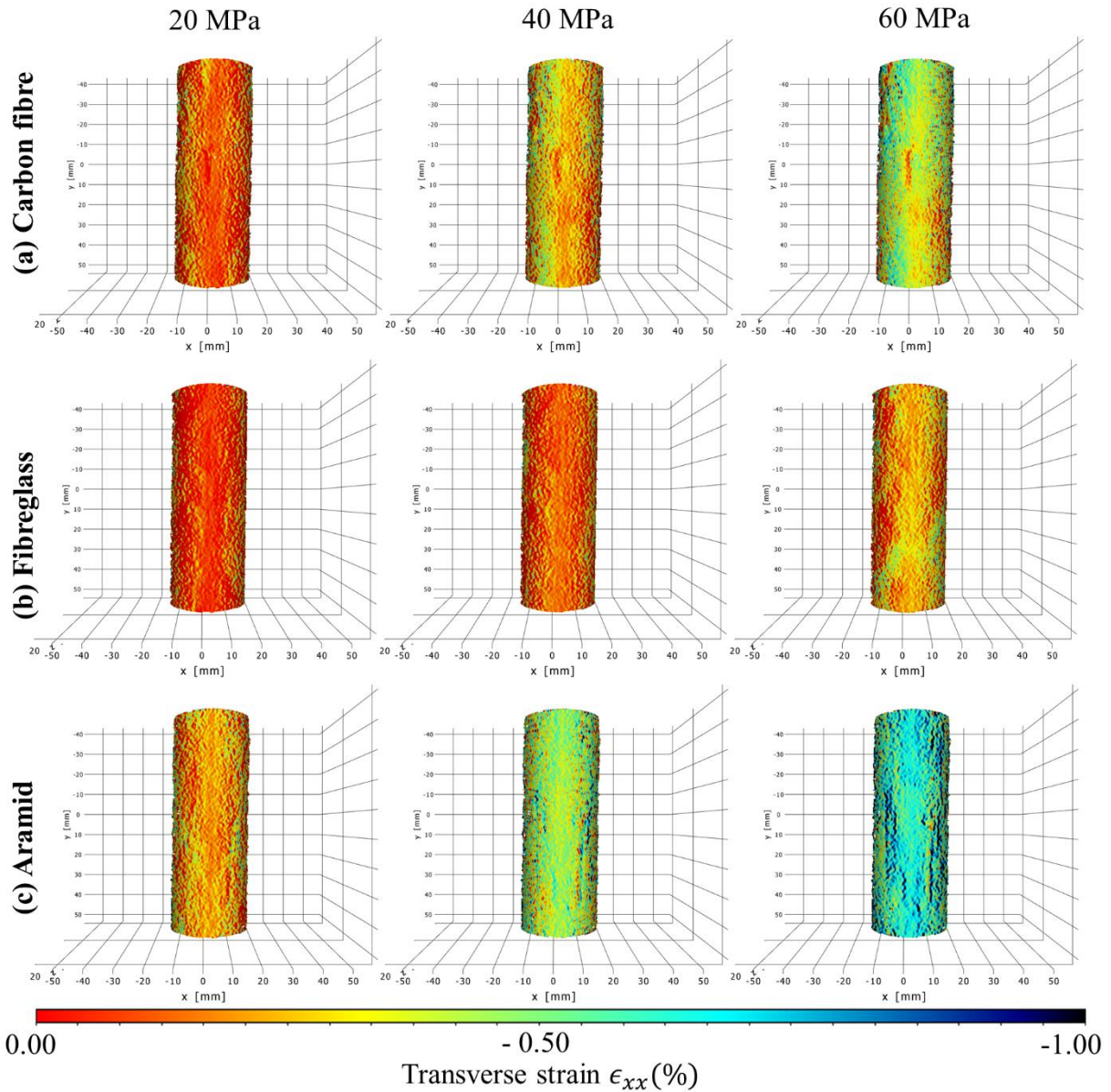
Figure 13: 3D representation of transverse strain distribution on three types of braids at low-stress states. Sample images show the three-dimensional strain distribution for the tubular braids (a) Carbon fibre (b) Fiberglass (c) Aramid. Sample stress of 20, 40 and 60 MPa are visualized.

3.2.3 $\epsilon_{xx} - \epsilon_{yy}$ curves, stiffness and ultimate tensile strength

The transverse strain versus longitudinal strain curves for all samples are shown in Figure 14. This figure is plotted for the elastic zone of the stress-strain curve of samples shown in Figure 10. The linear behaviour of the $\epsilon_{xx} - \epsilon_{yy}$ curves indicate uniform deformation of samples during tensile test strokes for all the braids. A similar conclusion on $\epsilon_{xx} - \epsilon_{yy}$ plots was stated in [26].

28

The uniform deformation of all samples indicates uniform epoxy resin impregnation to the fibres. The uniform distribution of matrix in braid preform demonstrates a consistent manufacturing technique was used to produce braids in this study.
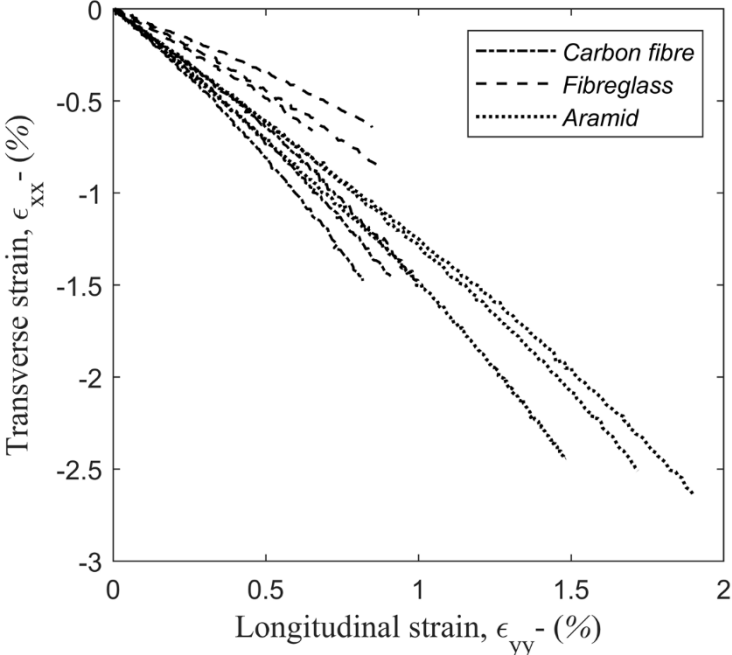
Figure 14: $\epsilon_{xx} - \epsilon_{yy}$ curves for carbon fibre, fibreglass and aramid TBCs.

Figure 15 shows the axial load plots versus crosshead displacement of the test frame for all samples. This figure is plotted for the elastic zone of the stress-strain curve of samples shown in Figure 10. Figure 15 shows that the load increases almost linearly with displacement for all the braids in the elastic deformation zone.
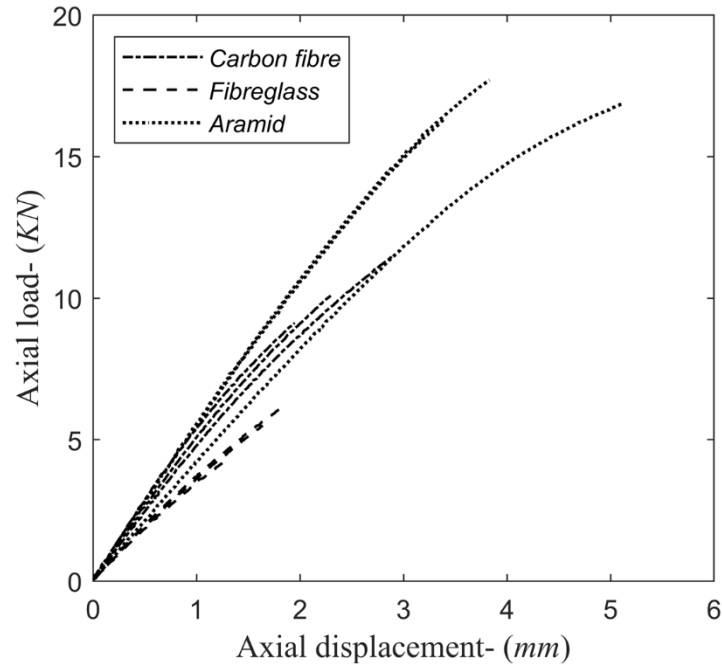
Figure 15: Axial load versus crosshead displacement for carbon fibre, fibreglass and aramid TBCs.

The slope of the curves in Figure 15 shows the axial stiffness of manufactured TBCs. The magnitude of axial stiffness for carbon fibre, fibreglass and aramid braids are 4.67 ± 0.38KN/mm, 3.51 ± 0.05KN/mm and 4.67 ± 0.86KN/mm, respectively. The carbon fibre and aramid braids showed almost equal axial stiffness and higher values than fibreglass braids. However, fibreglass braids showed consistent behaviour for their stiffness magnitude.

The ultimate tensile strength is the stress that each sample failed and fractured into two separate pieces at the end of the test stroke. The magnitude of ultimate tensile strength for carbon fibre, fibreglass, and aramid braids is 344.37 ± 4.48MPa, 298.66 ± 18.08MPa 367.30 ± 51.81MPa, respectively. The ultimate strength results demonstrate that aramid braids have the highest ultimate tensile strength than carbon fibre and fibreglass braids. Ultimate tensile strength for carbon fibre braid is higher than fibreglass braids. Carbon fibre braids showed consistent values for ultimate tensile strength with minimal variation relative to aramid and fibreglass ones.

The variations in magnitudes for stiffness and ultimate tensile strength can be due to geometrical parameters of braids such as braid angle and yarn width. The geometrical characteristic of braids can have a significant impact on the mechanical characteristics of braids.

30

For example, aramid braids have the highest variation in magnitude of stiffness and fibreglass braids have the lowest, which corresponds to the yarn width variation of braids measured and demonstrated in Table 5. This table shows that aramid braids have the highest, and fibreglass braids have the lowest yarn width variation. Ultimate tensile strength for braids depends on braid material and is highly dependent on braid geometry. Aramid has the highest ultimate tensile strength among the manufactured TBCs in this study due to having the lowest braid angle compared to other braid types (Table 5). Slight variation in braid angle can significantly impact the mechanical behaviour of braids. Besides braid angle and yarn width, fiber volume fraction and errors in the manual impregnation process can also alter braids' mechanical properties.

3.2.4 Failure analysis of TBCs in tension

Figure 16 demonstrates 3D DIC and raw images for carbon fibre, fibreglass and aramid braids, respectively, at ultimate tensile strength and right after the failure occurs. According to these figures, failure occurs at locations where there are high axial strain concentrations. These figures show the significant benefit of the 3D DIC technique that readily measures the failure location and observes the strain concentration on loaded specimens; however, this observation is not possible using conventional measurement techniques like strain gauges. According to raw images shown in these figures, it is difficult to visually determine the exact failure location and fracture surface by examining the raw images alone.
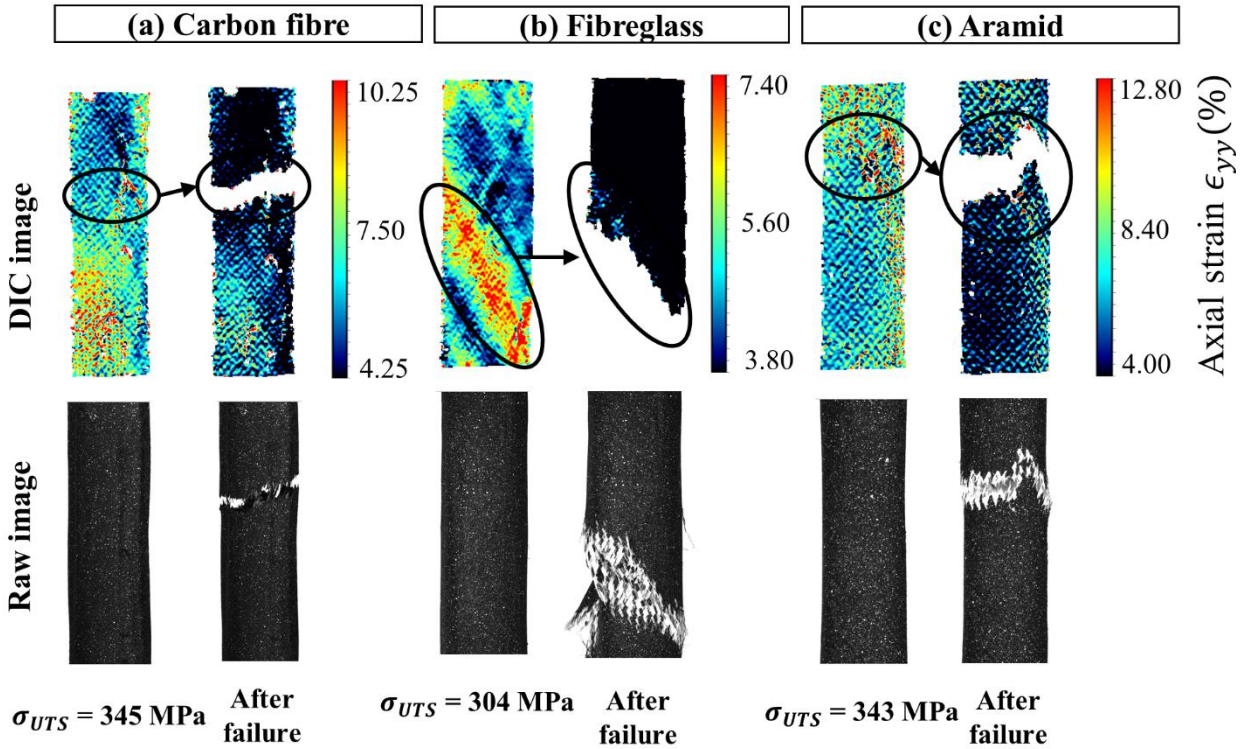
Figure 16: Example 3D DIC and raw images for carbon fibre braid right before and after failure. 3D DIC strain fields show the strain concentrations before failure at UTC

Figure 17 shows the failure modes for all the nine carbon fibre, fibreglass and aramid specimens. The failure codes used for these fractures are determined according to ASTM D3039 [41]. The failure code consists of three letters, the first letter indicates the first letter of failure type, the second one indicates the first letter of failure area, and the last one indicates the first letter of failure location. Two carbon fibre braids and all the aramid braids had Lateral failure type. The fibreglass braids had an Angled failure type. All fibreglass and aramid braids and two carbon fibre braids failed in the Gage area of the specimens and at the Middle location of braids. Therefore, the failure code for fibreglass, aramid and two carbon fibre braids became to be AGM, LGM and LGM, respectively. The other carbon fibre braid failed from the end tab epoxy. Therefore, its failure code is GIT, which means Grip/tab failure type, Inside grip/tab and the Top location of the braid. It is predicted that if the bonding were suitable for this carbon fibre braid, it would have the same LGM failure code as the other two carbon fibre braids. More details on failure codes are provided in ASTM D3039 [41]. There are few studies and data available to investigate the fracture surface of TBCs. Fracture surface analysis requires techniques like scanning electron microscopy.
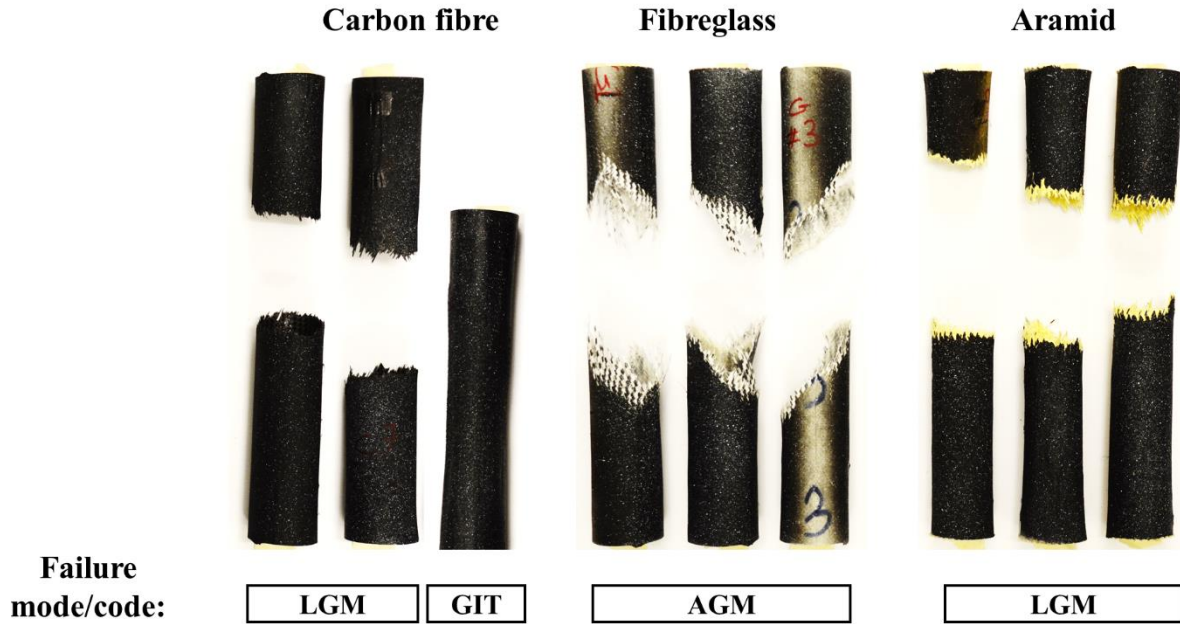
Figure 17: Images of all fractured specimens with their failure codes according to ASTM D3039. The failure code consists of three letters, the first letter stands for failure type, the second one stands for the failure area, and the last one shows the failure location. LGM: Lateral, Gage, Middle. GIT: Grip/tab, Inside grip/tab, Top. AGM: Angled, Gage, Middle.

3.3   Combined loading experiments

3.3.1   Shear strain behavior

Nine TBCs (three aramid, three fibreglass, three carbon) were subjected to combined tension-torsion loading. All the braids were preloaded to 40MPa axial stress. All samples behaved elastically under a 40MPa tensile stress since it was a stress magnitude in the linear region of stress-strain curves of all nine braids. After preloading axially to 40MPa, braids were twisted in rotational control mode that caused shear stress(τ_{xy}) and shear strain (ϵ_{xy}) in braids.

Shear stress on braids was determined using Equation (8). In this equation, T is the applied torque on braids measured by the test machine controller, D_i is the inner diameter and D_o is the outer diameter of braids that were measured using a micrometer. Shear stress is plotted versus torsional angle, θ_T, in Figure 18 when the torsional angle increases at a constant rate from $0°$ to $18°$. The negative sign of shear stress is due to the direction of applied torque from the lower crosshead. As plots in Figure 18 shows, the magnitude of shear stress initially increases linearly in all types of braids as the crosshead is rotating. After a few degrees of rotation from the lower crosshead, the linear region of plots for all braids ends sharply at different magnitudes of shear stress. In this study, the failure of braids in combined loading is considered at the end of the linear

33

region displayed in Figure 18 and the maximum shear stress, τ_{max}, is considered the shear stress corresponding to this point. The maximum shear stress for carbon fibre, fibreglass and aramid braids under combined loading are -48.81MPa ± 10.83MPa, -38.84MPa ± 5.81MPa and -51.16MPa ± 3.06MPa, respectively. The carbon fibre and aramid braids showed almost equal maximum shear stress and higher magnitudes than fibreglass braids. The variation in maximum shear stress is the highest for fibreglass and lowest for aramid braids. This variation can be related to the variation of braid angles that is shown in Table 5. According to this table, fibreglass has the highest variation in braid angle, and aramid has the lowest. According to Figure 18, one carbon fibre and one fibreglass braid show slightly strange behaviour so that their shear stresses have a second peak after showing the sharp drop in their curves. This behaviour can be due to poor/rich resin areas in the braids, although the shrink tape technique was used to minimize these irregular resin distributions.

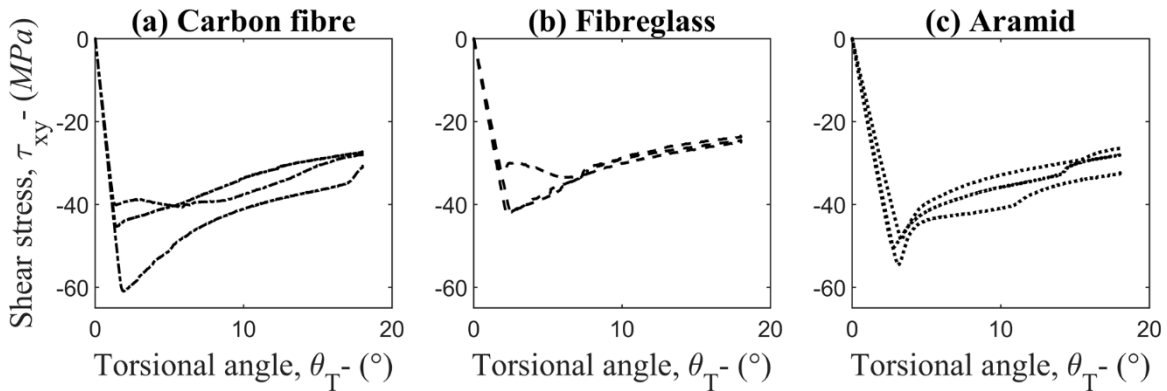$$\tau_{xy} = \frac{32 \, T \, D_o}{\pi \, (D_o^4 - D_i^4)} \qquad (8)$$

Figure 18: The relation between induced shear stress, τ_{xy}, while torsional angle, θ_T, increases on the tubular braids (a) Carbon fibre (b) Fiberglass (c) Aramid. The first sharp drop of these curves is considered as the maximum shear stress, τ_{max}.

The shear strain, ϵ_{xy}, was determined using the equation:

$$\epsilon_{xy} = \epsilon_{yx} = \frac{1}{2}\left(\frac{\partial u}{\partial y} + \frac{\partial v}{\partial x}\right) \qquad (9)$$

where u and v represent the displacement vector fields measured using the 3D DIC strain measurement technique in x and y directions. Figure 19 represents example 2D images of shear strain distributions on the surface of carbon fibre, fibreglass and aramid braids while experiencing combined loading. Figure 19-(i) shows the shear strain on braids at every increase of 5MPa in shear stress magnitude beginning from -5MPa to -30MPa for all braids. Figure 19-(ii) shows the strain distribution of braids at maximum shear stress (τ_{max}) where braid failure occurs. According to this figure, braids are experiencing non-uniform shear strain distribution due to the undulating structure of braided composites. Figure 19 also demonstrates the shear strain variations corresponding to the dark horizontal line in the middle of the braids at maximum shear stress. These strain variations show significant fluctuating strains along the dark line. According to these strain variations, it is observed that the shear strain period corresponds to the period of braid yarns. Similar observations were seen in a 3D DIC study by Melenka *et al.* [6] on TBCs examined in torsion loading.
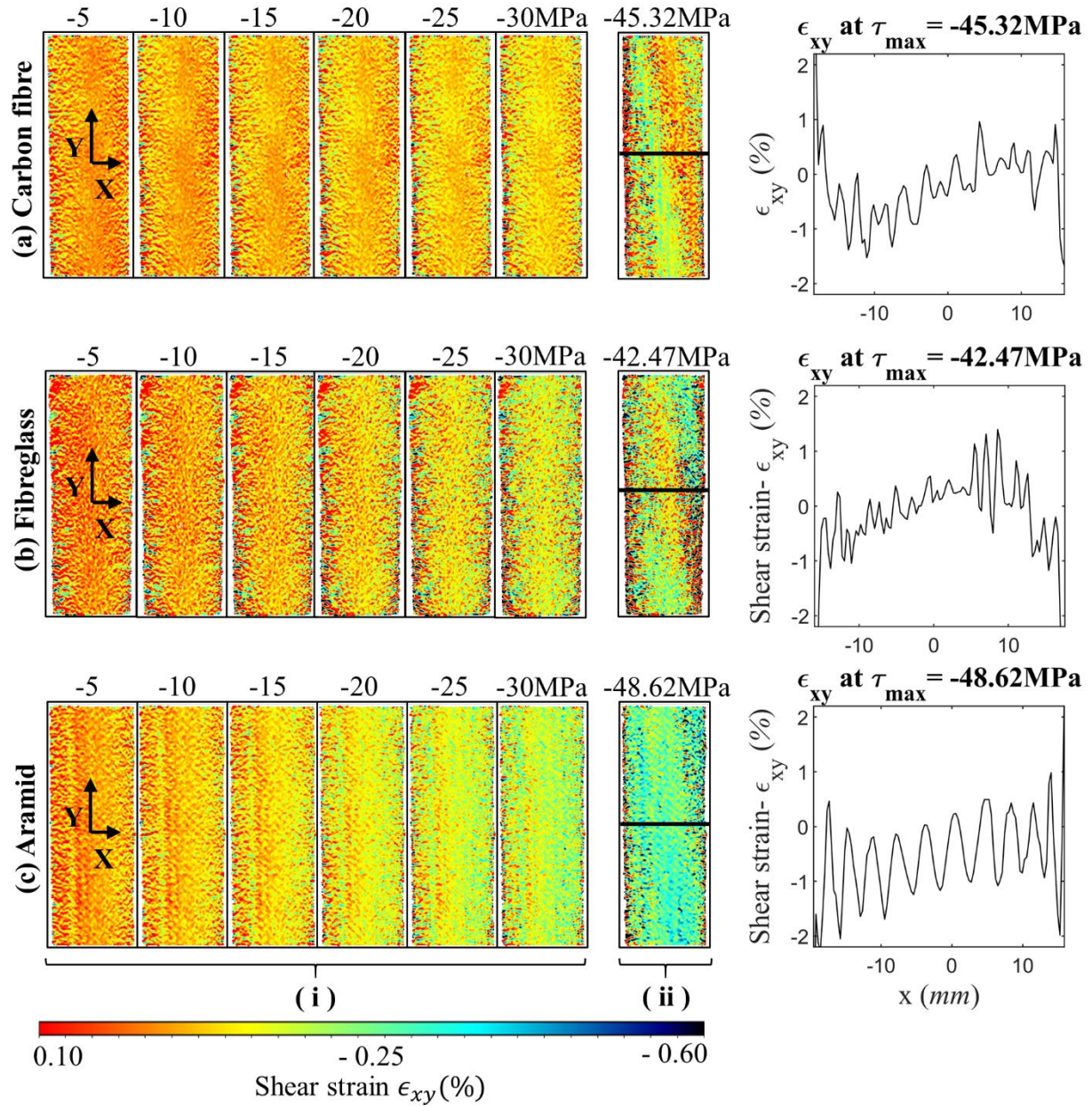
Figure 19: Images show the two-dimensional shear strain distribution (ϵ_{xy}) for the example tubular braids (a) Carbon fibre (b) Fiberglass (c) Aramid. i) shows colour map shear strain on braids for stress range of -5 MPa to -30 MPa with increasing steps of -5 MPa. ii) shows colour map shear strain on braids at maximum shear stress (τ_{max}) values. Shear strain distribution at maximum shear stress along the horizontal dark line at the middle of samples is also plotted.

3.3.2 *Failure analysis of TBCs in combined loading*

Figure 20 shows how the first principal plane angle, θ_{P_1}, changes during the rotation of crosshead, θ_T. According to Figure 18 and Figure 20, the first principal plane angle keeps increasing linearly for different braids as the crosshead is rotating, and shear stress is linearly increasing on braids. Considering Figure 18 and Figure 20, the linear increase of the first principal plane angle ends when the braid experiences its maximum shear stress. The maximum angle of the

first principal plane before the sharp drop of curves in Figure 20 is called the maximum principal plane angle, $\theta_{P_{max}}$. It should be reminded that the second principal plane angle (θ_{P_2}) behaves same as the first plane but with a shift of 90°, thus it is not plotted and compared.
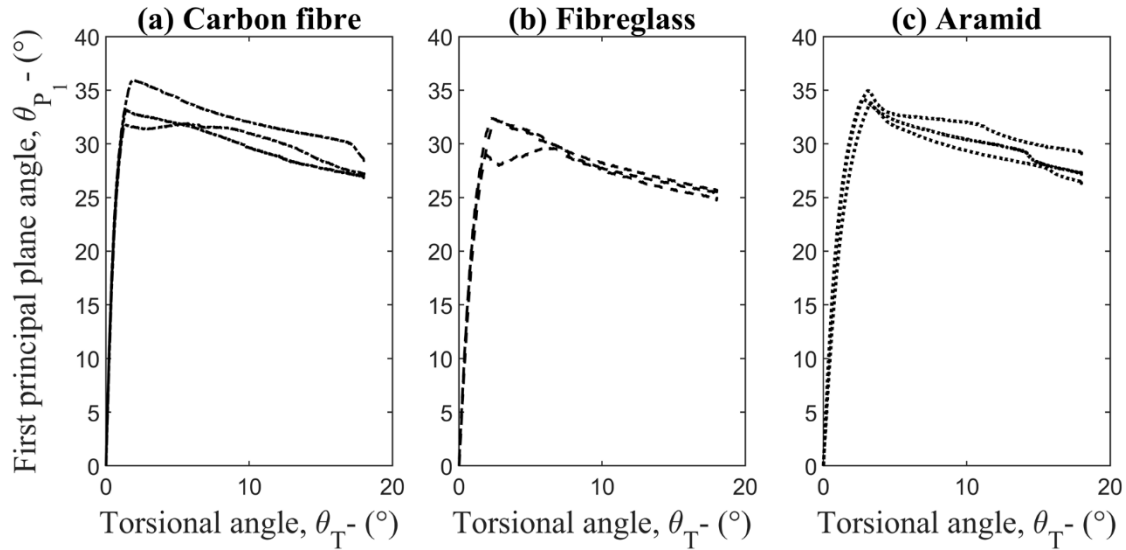

Figure 20: Changes in the first principal plane angle (θ_{P_1}) while torsional angle increases for the tubular braids (a) Carbon fibre (b) Fiberglass (c) Aramid.

The maximum principal plane angle is compared to the braid angles of TBCs using bar plots in Figure 21. The average maximum principal plane angles are $33.60° \pm 2.11°$, $31.22° \pm 1.89°$ and $34.30° \pm 0.58°$ for carbon fibre, fibreglass and aramid braids, respectively. Braid angles are listed in Table 6 for different groups of braids. According to Figure 21, the braid angle of braids is very close but a few degrees lower than the maximum principal plane angle for all three groups of specimens. To explain this difference, it must be reminded that the braid angle plotted in Figure 21, which is the angle between yarn direction and the longitudinal direction of braid, was measured when the braids were in unloaded condition. However, the braid yarns under combined loading are straightened in the preloading stage of the experiment and then tilted for a few degrees when the braids are experiencing their maximum shear stress because of the crosshead rotation. According to Figure 20, at the maximum principal plane angle, the lower crosshead has rotated $1.60° \pm 0.28°$, $2.22° \pm 0.39°$ and $3.07° \pm 0.25°$ for carbon fibre, fibreglass and aramid braids, respectively. This straightening and tilting results in a few degrees increase in the braid angle when the braid is maximum shear stress under combined loading. This increase in braid angle due to straightening and tilting is overlooked in the comparison made in Figure 21 as the braid angles were measured before sample loading. Performing braid angle measurement is not possible when

37

braids are under loading because they are painted and speckled for DIC measurement purposes. Thus, if the loading effect on the final orientation of yarns was measured, the new braid angle of loaded braids is anticipated to be almost the same as the maximum principal plane angle, not a few degrees lower than it. Therefore, it can be argued that at $\theta_{P_1} = \theta_{Pmax}$, θ_{P_1} is equal to θ_b.
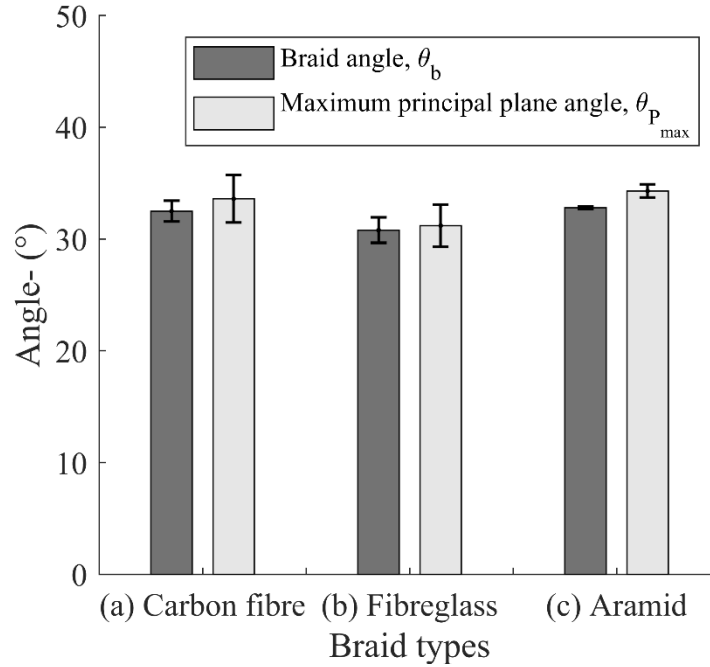

Figure 21: Comparison of the braid angle (θ_b) with the maximum principal plane angle (θ_{Pmax}) for the tubular braids (a) Carbon fibre (b) Fiberglass (c) Aramid.

Stresses acting on an example point O on the braid along the principal directions 1 and 2 are shown in Figure 5-(iii) when the braid is experiencing its maximum shear stress at $\theta_{P_1} = \theta_{Pmax} = \theta_b$. As shown in this figure, the principal planes are at angles of θ_{Pmax} and $\theta_{Pmax} + 90°$. Figure 5-(iii) demonstrates the equivalence of the maximum principal plane angle and braid angle. This figure shows that principal planes at θ_{Pmax} and $\theta_{Pmax} + 90°$ are along and perpendicular to yarn direction, respectively. Therefore, the principal stresses are acting perpendicular to the yarns in direction 1 and along the yarns in direction 2 at θ_{Pmax} and $\theta_{Pmax} + 90°$, respectively. Plugging in the $\theta_{P_1} = \theta_{Pmax}$ in equations (3) and (4), the magnitude and direction of principal stresses at $\theta_{Pmax} = \theta_b$ are determined. Equation (3) gives the principal stress in direction 1, σ_1, at principal plane of θ_{Pmax} as a compression stress and perpendicular to the braid yarns. Equation (4) gives the principal stress in direction 2, σ_2, at principal plane of $\theta_{Pmax} + 90°$ as a tension stress along the

yarn path. The direction of σ_1 and σ_2 on the braid yarns are shown in Figure 5-(iii). The averaged values of σ_1 and σ_2 for three groups of braids are illustrated with bar plots in Figure 22. Compressive principal stresses are -32.86MPa ± 10.05MPa, -23.75MPa ± 5.12MPa and -34.93MPa ± 2.87MPa for carbon fibre, fibreglass and aramid TBCs, respectively. Tensile principal stresses are 72.84 MPa ± 10.10 MPa, 63.73 MPa ± 5.08 MPa and 74.96 MPa ± 2.82 MPa for carbon fibre, fibreglass and aramid TBCs, respectively.
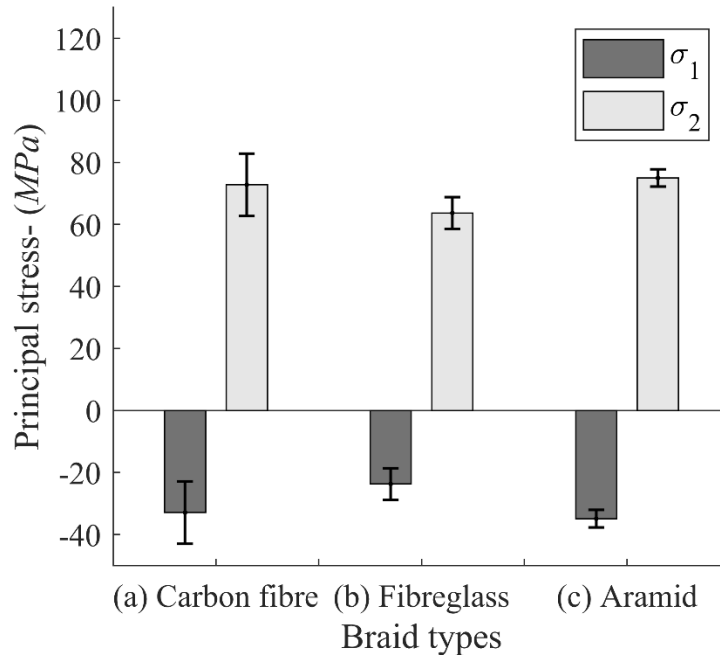

Figure 22: Demonstration of principal stresses on braids for the tubular braids (a) Carbon fibre (b) Fiberglass (c) Aramid. Principal stresses in direction 1 are in compression, and in direction 2 are in tension.

Considering the orientation of principal stresses on braid at its maximum principal plane angle and knowing that braid is showing failure behaviour at the same torsional angle corresponding to its maximum principal plane angle (Figure 18 and Figure 20), it can be argued that a braid under combined loading fails when the principal stresses are oriented perpendicular and parallel to the braid yarns. This means that when the braid is under combined loading and plane stress condition exists, braid failure occurs once the principal stresses on braid elements are introducing in planes that are along and perpendicular to braid yarns. In this case, significant matrix failure occurs, and the yarns are compressed and pulled by σ_1 and σ_2, respectively, without any induced shear stress

from the matrix on yarns as there is zero shear stress in principal directions. The signs of matrix failure are visible in Figure 18 when the linear increase of shear stress on braids stops and drops significantly at the torsional angle where $\theta_{P_{max}} = \theta_b$.

The only similar study that has studied TBCs under combined loading is the paper by Harte and Fleck. However, they had a different analysis focus and used conventional strain gauges for strain measurement purposes. Harte and Fleck analyzed fibreglass TBCs under combined tension-torsion loading to explore their failure on the stress path. Specimens had braid angles of 23°, 40° and 55°. They applied combined loading by holding a predetermined tensile force on the specimen within its uniaxial elastic limit and then, using the rotation control mode, twisted the sample to failure. They found that strain response was almost linear elastic to failure. Furthermore, they realized that the failure mode of braids is highly dependent on the braid angle. For $\theta_b = 55°$, braid failed due to micro buckling; however, for the braid of $\theta_b = 23°$, failure occurred because of fibre fractures. Failure of the braid with $\theta_b = 40°$ was a combination of two previous cases. One set of fibre tows failed in micro buckling, and the tows in bias direction failed due to fibre fracture. Harte and Fleck did not study the principal stresses for braids under combined loading. They were only focused on fibreglass braids and did not use any contact-free measurement technique.

3.3.3 Buckling behaviour of braids

Braids under combined axial/torsional loading showed surface deformation and demonstrated buckling as the torsional angle increased. Figure 23 shows example surface height profiles of braids generated using DIC deformation vector fields at three different stages of combined loading. These profiles are plotted along the dark horizontal line in the middle of the braids shown in Figure 19. Figure 23 shows the braid surface at three stages of the experiment using three types of lines. Line (i) shows the braid while no load is exerted on it. Line (ii) shows the surface of the braid when it has reached its maximum shear stress (τ_{max}). Crosshead torsional angle (θ_T) is mentioned at this stage for each braid type. As line (ii) illustrates, at this stage, buckling has slightly begun to propagate in the braid as the surface has deformed a little from its unloaded state. As the torsional angle increases, the buckled surface becomes more evident. To show the progressed buckled profile of the braid, line (iii) is plotted. Line (iii) shows the surface profile at a torsional angle of two degrees higher than the state of the braid surface showed by line (ii). Two degrees difference

was sufficient to show a well-developed buckled surface while still having the braid in the complete focus of cameras without losing correlation.
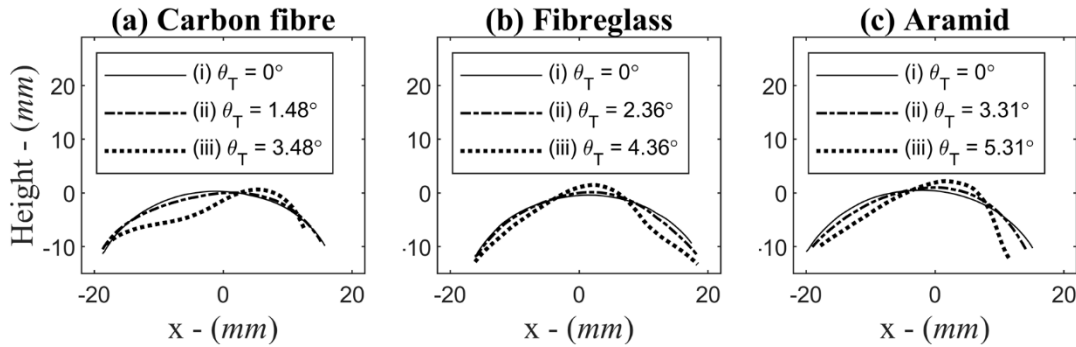

Figure 23: Surface height profiles at three loading stages for example, tubular braids (a) Carbon fibre (b) Fiberglass (c) Aramid as a demonstration of the buckling process. Line (i) shows the unloaded braid. Line (ii) shows the braids at maximum shear stress (τ_{max}). Line (iii) shows the braid when the torsional angle (θ_T) has increased for two more degrees from the maximum shear stress loading stage so that a progressed buckled surface can be visible.

Example surface of deformed braids in z-direction generated using the DIC technique at maximum shear stress is displayed in Figure 24. The richer shades of blue and reds show the braid has displaced negatively and positively in the z-direction, respectively. The displayed surfaces in Figure 24 clearly show that braids have started their buckling process at this loading stage. Braid surface profiles shown with line (ii) in Figure 23 corresponds to braids shown in Figure 24 that the braid is at its maximum shear stress.
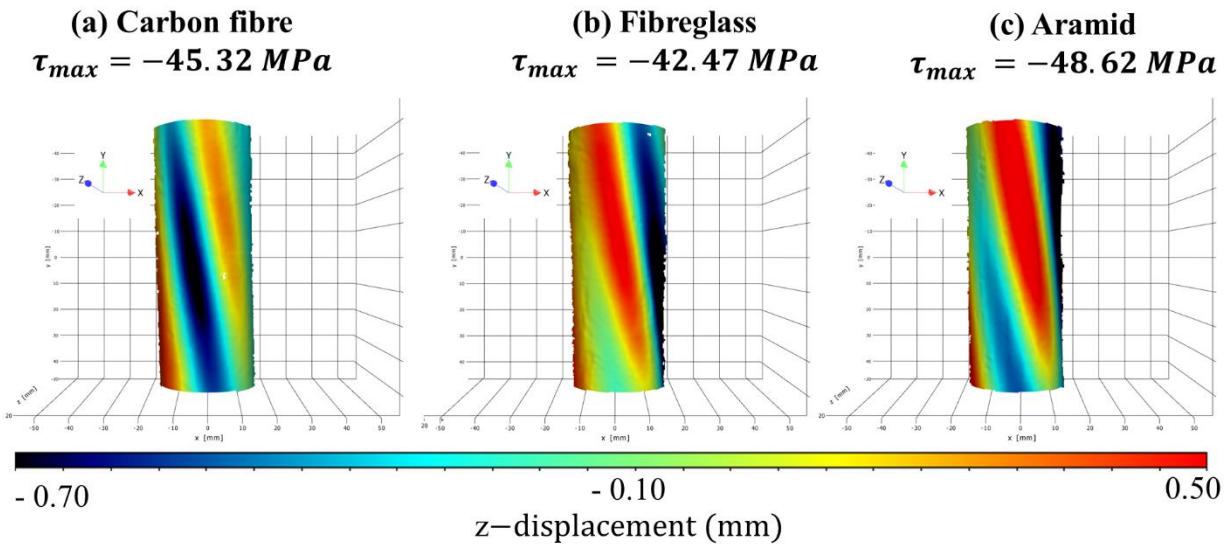
Figure 24: Example illustration of deformed braid surface in the z-direction at maximum shear stress (τ_{max}) for the tubular braids (a) Carbon fibre (b) Fiberglass (c) Aramid. According to this figure, the initial buckling of braids at this stage of loading is evident.

Example deformed braids at the end of combined loading experiments at eighteen degrees of crosshead rotation are demonstrated in Figure 25. Figure 25-(i) shows the braids have buckled significantly at the end of the combined loading test stroke. The DIC image of the portion of braid in the FOV of cameras in Figure 25-(i) is shown in Figure 25- (ii) for different groups of braids. According to this figure, carbon fibre, fibreglass and aramid braids have shown similar bucking shapes under combined loading. This figure shows the front side of the braids. If we consider buckled shape for the right, left, and behind views of the braids identical to their front view, a bucking mode drawn in Figure 26 can be generated for all braids. Based on a study on bucking behaviour on thin-walled tubes [52], this is called mode 4 of buckling.
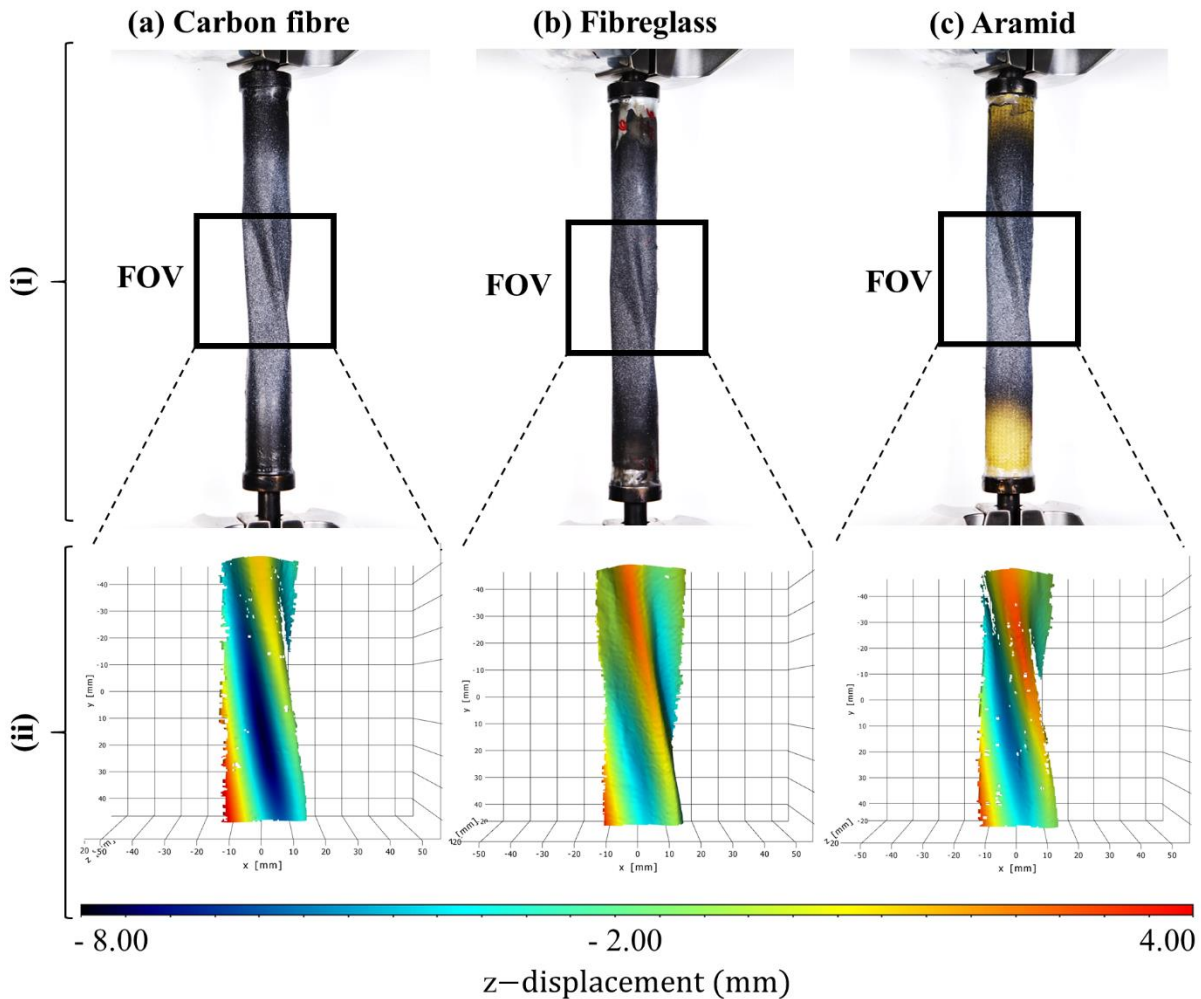
Figure 25: Illustration of buckled braids at the end of torsion stroke ($\theta_T = 18°$) for example tubular braids (a) Carbon fibre (b) Fiberglass (c) Aramid. (i) shows the raw images of buckled braids, and (ii) shows the DIC generated z-displacement colour maps of the braids in the FOV of cameras.
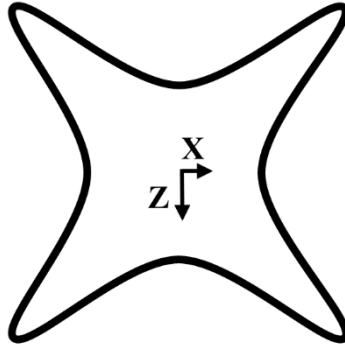

Figure 26: Proposed buckled shape for the carbon fibre, fibreglass and aramid TBCs under combined tension-torsion loading.

3.3.4 Stiffness of braids in combined loading

Torque magnitude versus torsional angle for braids under combined loading is shown in Figure 27. As the crosshead rotates at a constant rate, initially, torque increases on braids until a point that suddenly drops. This point is called the maximum torque, T_{max}. All the nine samples have shown a linear trend in their torque-torsional angle plot until the maximum torque. The slope of the linear region of Figure 27 is defined as the torsional stiffness of braids under combined loading. Carbon fibre braids have the highest torsional stiffness, and fibreglass braids have the lowest stiffness value under combined loading.
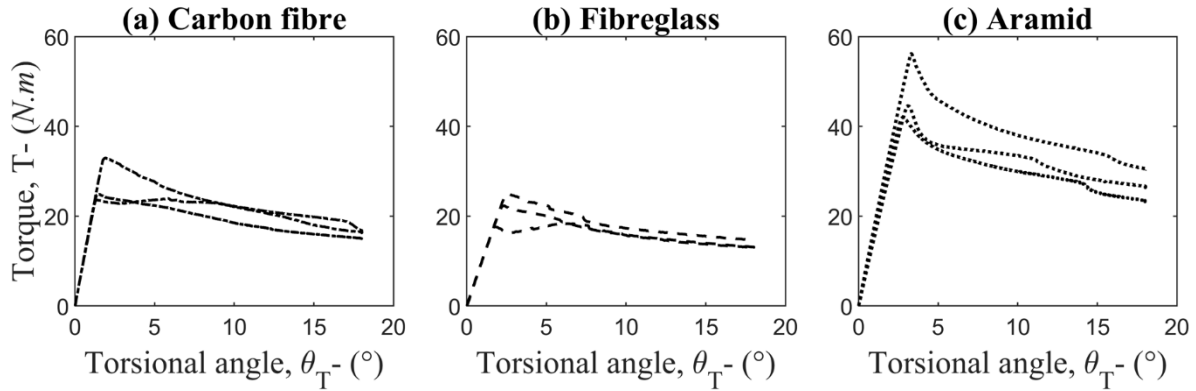
Figure 27: Plot of toque versus torsional angle for the tubular braids (a) Carbon fibre (b) Fiberglass (c) Aramid.

4. Conclusions

In this study, carbon fibre, fibreglass and aramid TBCs under combined tension-torsion loading were evaluated and compared. For this purpose, all manufactured TBC specimens were preloaded to specific tensile stress and then a torsional load was applied. Contact-free 3D DIC was utilized as the measurement technique. The maximum shear stress a TBC could endure while experiencing 40MPa tensile stress was determined for different braid fibres. The carbon fibre and aramid braids showed almost equal maximum shear stress and higher magnitudes than fibreglass braids.

Using the 3D DIC technique, shear strain fields for TBCs were generated in several loading stroke steps. According to the strain field results, braids have experienced non-uniform shear strain distribution due to braided composites' woven structure. Furthermore, it was observed that shear strain variations on braids had shown a period that corresponded to the braiding period of TBCs.

The failure behaviour of carbon fibre, fibreglass, and aramid TBCs was investigated and compared with specimens' braid angle. When braids are experiencing constant tension stress and shear stress increases on braid, failure occurs when the principal stresses in braid elements are acting perpendicular and along the braid yarn orientations. At this point, the linear increase of shear stress on braids stopped and dropped sharply, matrix failure occurred, and the braid could not endure any more load.

TBCs under combined loading demonstrated buckled surface when the torsional load was increasing on braids. Using the 3D DIC results, the deformed profile of the braid was plotted at different loading stages to see how the buckling progresses. According to 3D DIC results, braids

initiated their buckling process at the maximum shear stress. Furthermore, based on raw and 3D DIC images of braids at the end of the loading process, a symmetric four corner buckled surface profile was observed.

Lastly, by plotting the applied torque versus torsional angle for TBCs under combined tension-torsion, the torsional stiffness of braids was studied. All samples showed a linear trend in their torque-torsional angle plot until the maximum torque where the braids failed. Carbon fibre braids had the highest torsional stiffness, and fibreglass braids had the lowest torsional stiffness value under combined loading.

5. Declaration of competing Interest

The author(s) declare no conflicts of interest with respect to the research, authorship or publication of this article.

6. Acknowledgement

7. Data availability

The raw/processed data required to reproduce these findings cannot be shared at this time as the data also forms part of an ongoing study.

8. References

[1]   J. P. Carey, "1 - Introduction to braided composites," in *Handbook of Advances in Braided Composite Materials*, J. P. Carey, Ed. Woodhead Publishing, 2017, pp. 1–21.

[2]   J. Carey, A. Fahim, and M. Munro, "Design of braided composite cardiovascular catheters based on required axial, flexural, and torsional rigidities," *J. Biomed. Mater. Res. Part B Appl. Biomater.*, vol. 70B, no. 1, pp. 73–81, 2004, doi: 10.1002/jbm.b.30017.

[3]   J. A. [de O. Simões] and A. T. Marques, "Determination of stiffness properties of braided composites for the design of a hip prosthesis," *Compos. Part A Appl. Sci. Manuf.*, vol. 32, no. 5, pp. 655–662, 2001, doi: https://doi.org/10.1016/S1359-835X(00)00157-3.

[4]   B. Dauda, S. O. Oyadiji, and P. Potluri, "Characterising mechanical properties of braided

and woven textile composite beams," *Appl. Compos. Mater.*, vol. 16, no. 1, pp. 15–31, 2009, doi: 10.1007/s10443-008-9073-3.

[5]   A.-M. Harte and N. A. Fleck, "On the mechanics of braided composites in tension," *Eur. J. Mech. - A/Solids*, vol. 19, no. 2, pp. 259–275, 2000, doi: https://doi.org/10.1016/S0997-7538(99)00164-3.

[6]   G. W. Melenka and J. P. Carey, "Experimental analysis of diamond and regular tubular braided composites using three-dimensional digital image correlation," *J. Compos. Mater.*, vol. 51, no. 28, pp. 3887–3907, 2017, doi: 10.1177/0021998317695418.

[7]   C. Ayranci and J. Carey, "2D braided composites: A review for stiffness critical applications," *Compos. Struct.*, vol. 85, no. 1, pp. 43–58, 2008, doi: https://doi.org/10.1016/j.compstruct.2007.10.004.

[8]   T. Wehrkamp-Richter, R. Hinterhölzl, and S. T. Pinho, "Damage and failure of triaxial braided composites under multi-axial stress states," *Compos. Sci. Technol.*, vol. 150, pp. 32–44, 2017, doi: 10.1016/j.compscitech.2017.07.002.

[9]   L. Gong, X. Gao, H. Yang, Y. Liu, and X. Yao, "Design on the driveshaft of 3D 4-Directional carbon fiber braided composites," *Compos. Struct.*, vol. 203, pp. 466–473, Nov. 2018, doi: 10.1016/j.compstruct.2018.06.103.

[10]   W. Hao, Z. Huang, L. Zhang, G. Zhao, and Y. Luo, "Study on the torsion behavior of 3-D braided composite shafts," *Compos. Struct.*, vol. 229, p. 111384, 2019, doi: https://doi.org/10.1016/j.compstruct.2019.111384.

[11]   G. Zhao, L. Zhang, C. Tang, Y. Zhou, W. Hao, and Y. Luo, "Experimental study on the torsion behavior of a 3D 4-directionally braided composite shaft using DIC and AE," *Polym. Test.*, vol. 72, pp. 122–131, 2018, doi: https://doi.org/10.1016/j.polymertesting.2018.10.016.

[12]   C. Unlusoy and G. W. Melenka, "Flexural testing of cellulose fiber braided composites using three dimensional digital image correlation," *Compos. Struct.*, vol. 230, no. August, p. 111538, 2019, doi: 10.1016/j.compstruct.2019.111538.

[13]   G. Yu, X. Gao, and Y. Song, "Experimental investigation of the tension-torsion coupling

behavior on needled unidirectional C/SiC composites," *Mater. Sci. Eng. A*, 2017, doi: 10.1016/j.msea.2017.04.028.

[14]   G. W. Melenka *et al.*, "3 - Manufacturing processes for braided composite materials," in *Handbook of Advances in Braided Composite Materials*, J. P. Carey, Ed. Woodhead Publishing, 2017, pp. 47–153.

[15]   S. Nawaz, P. Potluri, M. Gautam, and S. S. Roy, "Study of braid toplogy and effect of braid pattern on composite properties," in *ICCM International Conferences on Composite Materials*, 2013, vol. 2013-July, pp. 689–695.

[16]   C. Ayranci, D. Romanyk, and J. P. Carey, "Elastic properties of large-open-mesh 2D braided composites: Model predictions and initial experimental findings," *Polym. Compos.*, vol. 31, no. 12, pp. 2017–2024, Dec. 2010, doi: 10.1002/pc.20999.

[17]   C. K. Leung, G. W. Melenka, D. S. Nobes, and J. P. Carey, "The effect on elastic modulus of rigid-matrix tubular composite braid radius and braid angle change under tensile loading," *Compos. Struct.*, vol. 100, pp. 135–143, 2013, doi: https://doi.org/10.1016/j.compstruct.2012.12.038.

[18]   A.-M. Harte and N. A. Fleck, "Deformation and failure mechanisms of braided composite tubes in compression and torsion," *Acta Mater.*, vol. 48, no. 6, pp. 1259–1271, 2000, doi: https://doi.org/10.1016/S1359-6454(99)00427-9.

[19]   G. W. Melenka and J. P. Carey, "Experimental analysis of diamond and regular tubular braided composites using three-dimensional digital image correlation," *J. Compos. Mater.*, vol. 51, no. 28, pp. 3887–3907, 2017, doi: 10.1177/0021998317695418.

[20]   Y. Chai *et al.*, "Damage evolution in braided composite tubes under torsion studied by in-situ X-ray computed tomography," *Compos. Sci. Technol.*, vol. 188, p. 107976, 2020, doi: https://doi.org/10.1016/j.compscitech.2019.107976.

[21]   B. Bruni-Bossio, C. Ayranci, J. P. Carey, T. Omonov, and J. Curtis, "Experimental testing of the tensile elastic properties of cellulose braided composites," *Compos. Part B Eng.*, vol. 166, no. October 2018, pp. 542–548, 2019, doi: 10.1016/j.compositesb.2019.02.052.

[22]   G. Yu, X. Gao, and Y. Song, "Experimental investigation of the tension-torsion coupling

behavior on needled unidirectional C/SiC composites," *Mater. Sci. Eng. A*, vol. 696, pp. 190–197, 2017, doi: https://doi.org/10.1016/j.msea.2017.04.028.

[23]   S. Amijima, T. Fujii, and M. Hamaguchi, "Static and fatigue tests of a woven glass fabric composite under biaxial tension-torsion loading," *Composites*, vol. 22, no. 4, pp. 281–289, 1991, doi: https://doi.org/10.1016/0010-4361(91)90003-Y.

[24]   A. Armanfard and G. Melenka, "Combined Loading Evaluation of Braided Composites," no. 3d Dic, p. 2020, 2020, doi: 10.32393/csme.2020.32.

[25]   B. Pan, L. Yu, Y. Yang, W. Song, and L. Guo, "Full-field transient 3D deformation measurement of 3D braided composite panels during ballistic impact using single-camera high-speed stereo-digital image correlation," *Compos. Struct.*, vol. 157, pp. 25–32, 2016, doi: https://doi.org/10.1016/j.compstruct.2016.08.017.

[26]   Y. Zheng *et al.*, "Tensile response of carbon-aramid hybrid 3D braided composites," *Mater. Des.*, vol. 116, pp. 246–252, 2017, doi: https://doi.org/10.1016/j.matdes.2016.11.082.

[27]   T. Wehrkamp-Richter, R. Hinterhölzl, and S. T. Pinho, "Damage and failure of triaxial braided composites under multi-axial stress states," *Compos. Sci. Technol.*, vol. 150, pp. 32–44, 2017, doi: https://doi.org/10.1016/j.compscitech.2017.07.002.

[28]   D. Zhang, S. Yu, G. Feng, X. Xiao, Q. Ma, and K. Qian, "Numerical Identification of Meso Length-Effect and Full-Field Edge-Effect of 3D Braided Composites," *Appl. Compos. Mater.*, vol. 25, pp. 1–22, 2017, doi: 10.1007/s10443-017-9657-x.

[29]   J. Cichosz, T. Wehrkamp-Richter, H. Koerber, R. Hinterhölzl, and P. P. Camanho, "Failure and damage characterization of (±30°) biaxial braided composites under multiaxial stress states," *Compos. Part A Appl. Sci. Manuf.*, vol. 90, pp. 748–759, 2016, doi: https://doi.org/10.1016/j.compositesa.2016.08.002.

[30]   B. Practices and U. Quanti, *A Good Practices Guide for Digital Image Correlation*, no. January. International Digital Image Correlation Society, 2018.

[31]   R. Elhajjar, S. Shams, and D. Kehrl, "Closed form solutions for predicting the elastic behavior of quasi-isotropic triaxially braided composites," *Compos. Struct.*, vol. 101, pp.

1–8, 2013, doi: 10.1016/j.compstruct.2012.12.036.

[32] Z. T. Kier, A. Salvi, G. Theis, A. M. Waas, and K. Shahwan, "Estimating mechanical properties of 2D triaxially braided textile composites based on microstructure properties," *Compos. Part B Eng.*, vol. 68, pp. 288–299, 2015, doi: https://doi.org/10.1016/j.compositesb.2014.08.039.

[33] "Braided Carbon Biaxial Sleeve." https://s3.amazonaws.com/cdn.fibreglast.com/downloads/00357.pdf (accessed Nov. 15, 2018).

[34] G. W. Melenka, C. M. Pastore, F. K. Ko, and J. P. Carey, "9 - Advances in 2-D and 3-D braided composite material modeling," in *Handbook of Advances in Braided Composite Materials*, J. P. Carey, Ed. Woodhead Publishing, 2017, pp. 321–363.

[35] W. S. Johnson, J. E. Masters, D. W. Wilson, J. Chen, T. M. McBride, and S. B. Sanchez, "Sensitivity of Mechanical Properties to Braid Misalignment in Triaxial Braid Composite Panels," *J. Compos. Technol. Res. - J Compos TECH RES*, vol. 20, 1998, doi: 10.1520/CTR10495J.

[36] G. W. Melenka, M. Ivey, and J. P. Carey, "2 - Working with the braided composite app," in *Handbook of Advances in Braided Composite Materials*, J. P. Carey, Ed. Woodhead Publishing, 2017, pp. 23–43.

[37] G. W. Melenka, E. Lepp, B. K. O. Cheung, and J. P. Carey, "Micro-computed tomography analysis of tubular braided composites," *Compos. Struct.*, vol. 131, pp. 384–396, 2015, doi: 10.1016/j.compstruct.2015.05.057.

[38] G. W. Melenka and J. P. Carey, "Development of a generalized analytical model for tubular braided-architecture composites," *J. Compos. Mater.*, vol. 51, no. 28, pp. 3861–3875, 2017, doi: 10.1177/0021998317695421.

[39] G. W. Melenka, A. J. Hunt, C. M. Pastore, F. K. Ko, and J. P. Carey, "4 - Advanced testing of braided composite materials," in *Handbook of Advances in Braided Composite Materials*, J. P. Carey, Ed. Woodhead Publishing, 2017, pp. 155–204.

[40] "ASTM E111 - 17 Standard Test Method for Young's Modulus, Tangent Modulus, and

Chord Modulus." https://www.astm.org/Standards/E111.htm (accessed Feb. 26, 2020).

[41]   D 3039/D3039M ASTM, "Standard Test Method for Tensile Properties of Polymer Matrix Composite Materials," *Annu. B. ASTM Stand.*, vol. 15.03, pp. 105–116, 2000, doi: 10.1520/D3039_D3039M-08.

[42]   M. A. Sutton, J.-J. Orteu, Image, and H. W. Schreier, "Image Correlation for Shape, Motion and Deformation Measurements," doi: 10.1007/978-0-387-78747-3.

[43]   LaVision GmbH, "Product-Manual DaVis StrainMaster 10.0 Item-Number(s): 1003017," 2018.

[44]   R. A. Naik, P. G. Ifju, and J. E. Masters, "Effect of Fiber Architecture Parameters on Deformation Fields and Elastic Moduli of 2-D Braided Composites," *J. Compos. Mater.*, vol. 28, no. 7, pp. 656–681, 1994, doi: 10.1177/002199839402800705.

[45]   F. Beer, E. R. Jr. Johnston, J. DeWolf, and D. Mazurek, *Mechanics of Materials*. McGraw-Hill Education, 2011.

[46]   A. K. Kaw, *Mechanics of composite materials*. CRC press, 2005.

[47]   C. K. Leung, G. W. Melenka, D. S. Nobes, and J. P. Carey, "The effect on elastic modulus of rigid-matrix tubular composite braid radius and braid angle change under tensile loading," *Compos. Struct.*, vol. 100, pp. 135–143, Jun. 2013, doi: 10.1016/j.compstruct.2012.12.038.

[48]   N. Chernov, "Circle Fit (Pratt method)," *MATLAB Central File Exchange. Retrieved April 28, 2020.*, 2020. .

[49]   J. Carey, M. Munro, and A. Fahim, "Longitudinal elastic modulus prediction of a 2-D braided fiber composite," *J. Reinf. Plast. Compos.*, vol. 22, no. 9, pp. 813–831, 2003, doi: 10.1177/0731684403022009003.

[50]   L. Xu, S. J. Kim, C.-H. Ong, and S. K. Ha, "Prediction of material properties of biaxial and triaxial braided textile composites," *J. Compos. Mater.*, vol. 46, no. 18, pp. 2255–2270, 2012, doi: 10.1177/0021998311431353.

[51]   G. W. Melenka and J. P. Carey, "Development of a generalized analytical model for

tubular braided-architecture composites," *J. Compos. Mater.*, vol. 51, no. 28, pp. 3861–3875, 2017, doi: 10.1177/0021998317695421.

[52] R. Gonçalves and D. Camotim, "Buckling behaviour of thin-walled regular polygonal tubes subjected to bending or torsion," *Thin-Walled Struct.*, vol. 73, pp. 185–197, 2013, doi: https://doi.org/10.1016/j.tws.2013.08.006.